Axial-Geometric Fermi-Arc Qubits

Converting Weyl-Node Chirality into a Noise-Orthogonal Superconducting Circuit

Rihaan Shah

July 2026

Abstract

This manuscript develops a superconducting-qubit architecture in which the Josephson element is a Weyl-semimetal weak link whose useful control coordinate is not an ordinary electromagnetic phase alone, but a strain-generated axial gauge field that couples with opposite sign to Weyl nodes of opposite chirality. The principal target material is trigonal $PtBi_2$, motivated by recent evidence for superconductivity localized on Fermi-arc surface states, by scanning tunneling results for elevated-temperature surface superconductivity, and by spin-resolved photoemission evidence that the relevant surface arcs are singly degenerate and spin polarized. The central hypothesis is the existence of an axial-geometric sweet manifold: a finite operating region in which the qubit transition frequency has suppressed first-order response to offset charge, ordinary flux, and electrostatic chemical-potential noise, while retaining a controllable derivative with respect to a selected strain mode. The proposal is deliberately conservative about protection. Band topology, suppressed backscattering in a nondegenerate surface channel, approximate chirality conservation, and protection of the logical circuit eigenstates are treated as distinct statements requiring distinct diagnostics.

The paper introduces a material-specific axial coupling tensor $\Lambda_{i,jk} = \partial b_i / \partial \epsilon_{jk}$, a projector-defined Fermi-arc participation ratio, a bulk-leakage ratio, a dimensioned and dimensionless noise-orthogonality ratio, and a topological retention score comparing matched Weyl and trivial controls. A microscopic route is given from strained first-principles electronic structure to Wannier interpolation, surface Green functions, Bogoliubov-de Gennes Josephson spectra, geometric capacitance, circuit quantization, and open-system rates. Minimal-model calculations are included to show how the diagnostics behave and to define falsifiable thresholds, but no fabricated $PtBi_2$ density-functional result is reported. The conclusion is mixed by design: axial-geometric operation is plausible only if Fermi-arc participation remains high, intervalley scattering remains below the superconducting and qubit scales, geometric capacitance competes with lithographic capacitance, and the predicted sweet region disappears in matched trivial controls.

Scope and evidence labels. Each result is labeled by its evidentiary status: A, analytically derived in this manuscript; M, numerically evaluated in the transparent minimal model in this manuscript; P, reproduced or constrained from published primary literature; E, estimated from published parameters; I, illustrative synthetic operating data used only to explain a protocol; and X, proposed experimental prediction. Figures are scientific schematics or minimal-model calculations with explicit parameters. No density-functional calculation for $PtBi_2$ has been executed here, and the material-specific first-principles values are therefore specified as a reproducible workflow and stopping criterion rather than as completed data.

Contents

1 Notation

Table 1: Notation used throughout the manuscript. Symbols are defined where first used in the main text; this table collects the recurring ones for reproducibility.

Symbol	Units or type	Meaning
χ	dimensionless	Weyl-node chirality, with $\chi = \pm 1$.
$\boldsymbol{b}_\chi$	inverse length	Momentum-space Weyl-node position for chirality χ.
$\boldsymbol{A}_5$	inverse length	Strain-induced axial vector potential that shifts nodes with opposite sign.
$\Lambda_{i,jk}$	inverse length	Axial coupling tensor $\partial b_i / \partial \epsilon_{jk}$.
ϵ_{jk}	dimensionless	Strain tensor component.
ϵ_{c}	dimensionless	Selected scalar strain-control mode used for gates and tuning.
φ	radians	Electromagnetic superconducting phase difference.
φ_5	radians	Effective axial phase generated by strain in the weak link.
Φ_{ext}	webers or Φ_0	Externally applied ordinary magnetic flux.
n_g	Cooper-pair charge units	Offset charge coordinate of the superconducting island.
μ	energy	Chemical potential relative to a chosen Weyl-node or arc reference.
E_ν	energy	BdG eigenenergy labeled by mode index ν.
F_{J}	energy	Junction free energy obtained from the BdG spectrum.
$I(\varphi)$	amperes	Microscopic current-phase relation.
U_{W}	energy	Weyl-material Josephson potential after integrating the current.
C_{geo}	farads	Geometric or adiabatic Josephson capacitance contribution.
C_{eff}	farads	Total effective capacitance entering phase dynamics.
E_C	energy	Charging energy $e^2/(2C_{\mathrm{eff}})$, possibly phase dependent.

Symbol	Units or type	Meaning
E_L	energy	Inductive energy of loop or superinductor embedding.
ω_{01}	angular frequency	Logical qubit transition frequency $(E_1 - E_0)/\hbar$.
α	angular frequency	Anharmonicity $\omega_{12} - \omega_{01}$.
P_{arc}	dimensionless	Projector-defined Fermi-arc participation ratio.
L_{bulk}	dimensionless	Bulk leakage ratio or non-surface participation.
$\mathcal{A}_5$	angular frequency per strain	Axial addressability, $\lvert\partial\omega_{01}/\partial\epsilon_{\mathrm{c}}\rvert$.
$\mathcal{R}_{\mathrm{NO}}$	convention dependent	Noise-orthogonality ratio comparing strain control to unwanted noise sensitivity.
Γ_{v}	inverse time	Intervalley or chirality-mixing scattering rate.
$S_\lambda(\omega)$	parameter^2/Hz	One-sided spectral density of noise parameter λ.
$\Delta_{\min}$	energy	Minimum superconducting gap on the current-carrying arc or weak-link spectrum.
$\mathcal{T}_m$	dimensionless	Normal-state transmission of channel m.
η_5	radians per strain	Device-level strain-to-axial-phase coefficient.

2 Introduction

Superconducting circuits normally suppress environmental sensitivity by engineering collective electromagnetic variables. The transmon, for example, trades charge dispersion against weakly reduced anharmonicity by increasing E_J/E_C [1]. Fluxonium, gatemons, Andreev qubits, and hybrid semiconductor circuits change the impedance, the weak-link spectrum, or the microscopic subgap states, but their control and dominant noise channels still largely live in the same electromagnetic parameter space. The architecture developed here asks whether a topological semimetal can provide a different kind of coordinate: a material control channel that is approximately orthogonal to ordinary charge and flux noise because it couples differentially to the chirality of Weyl nodes.

The physical ingredient is the axial gauge response of a Weyl semimetal. In a low-energy Weyl Hamiltonian, a perturbation that moves a node of chirality $\chi = +1$ in one direction and a node of chirality $\chi = -1$ in the opposite direction acts as an axial vector potential $\boldsymbol{A}_5$. Elastic strain is the most concrete realization because it changes bond lengths, crystal fields, and spin-orbit matrix elements in a way that can shift Weyl nodes in momentum space

[15, 16, 19]. An ordinary electromagnetic vector potential couples to charge in common mode. An axial gauge field couples with a sign set by chirality. A Weyl-semimetal Josephson element can therefore, in principle, distinguish an intentional strain-control drive from a broad class of ordinary electromagnetic fluctuations.

The material motivation has sharpened substantially. $PtBi_2$ has been reported to host superconductivity concentrated in topological Fermi-arc surface states [8], and separate scanning tunneling measurements report surface superconductivity in trigonal $PtBi_2$ at elevated temperature [9]. A July 2, 2026 spin-resolved photoemission preprint reports singly degenerate, spin-polarized Fermi arcs with strong surface-termination dependence [10]. These results do not by themselves create a protected qubit. They do, however, make a material-specific theory of superconducting Fermi-arc weak links timely. The measured termination dependence is especially important for circuit design because a flat arc with enhanced surface density of states and a steep arc with stronger bulk hybridization are not interchangeable weak links.

The novelty pursued here is not the claim that a Weyl semimetal can be placed in a superconducting circuit. A flux-tunable transmon-like circuit based on T_d-$MoTe_2$ Josephson junctions has already been reported [13]. Nor is the novelty merely that Fermi arcs can carry supercurrent, since Fermi-arc-mediated Josephson transport is already being analyzed theoretically [14]. The proposed contribution is a complete chain from crystal topology to circuit response: material-specific axial coupling, Fermi-arc participation, microscopic Andreev spectra, geometric capacitance, circuit quantization, and open-system noise. The central question is whether those ingredients can produce a finite sweet region with useful strain addressability rather than a single fine-tuned sweet point.

The manuscript is intentionally written with failure modes in the foreground. Weyl nodes and Fermi arcs are band-topological objects. A nondegenerate surface arc may reduce ordinary backscattering. Chirality may be approximately retained when disorder is smooth on the inverse node-separation scale. A logical qubit is protected only when the two lowest circuit eigenstates acquire suppressed transition-frequency sensitivity to the relevant noise operators. These four levels are related but not equivalent. Confusing them would overstate the proposal and obscure the measurements that could falsify it.

3 Weyl and Dirac Semimetals as Quantum-Circuit Materials

A Weyl point is a linear band touching that behaves as a Berry-curvature monopole in momentum space. Its topological charge is

$$C_{\mathrm{W}} = \frac{1}{2\pi} \oint_{S^2} \boldsymbol{\Omega}_n(\boldsymbol{k}) \cdot \mathrm{d}\boldsymbol{S}, \tag{1}$$

where S^2 encloses only the node and $\boldsymbol{\Omega}_n$ is the Berry curvature of the occupied band or band subspace. The Nielsen-Ninomiya constraint requires the net chirality in the Brillouin zone to vanish, so Weyl nodes occur in pairs or larger multiplets. On a surface, projections of nodes with opposite net chirality can be connected by open Fermi arcs. These statements are now standard in the theory and experiments of Weyl and Dirac semimetals [2, 3, 4, 5, 6, 7].

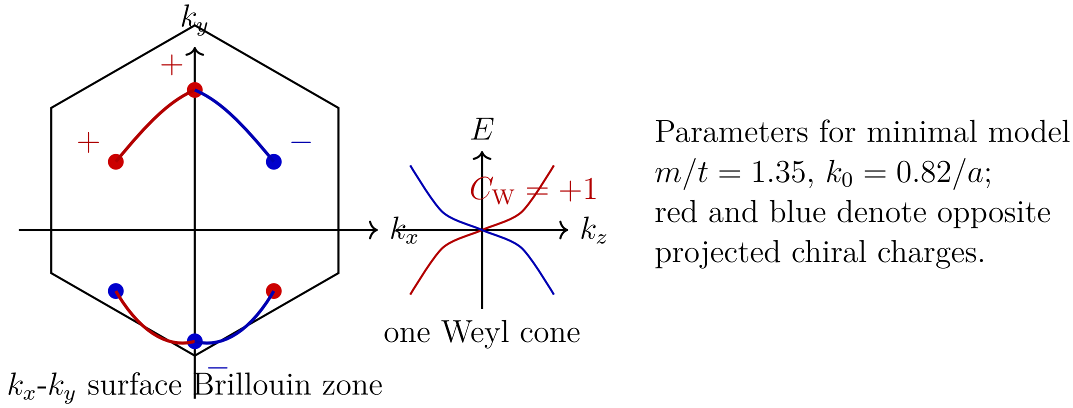

Figure 1: Evidence class M. Crystal and projected-node schematic for the minimal time-reversal-paired Weyl model used throughout the paper. The left panel shows projected Weyl nodes and arc connectivity on a hexagonal surface Brillouin zone. The right panel shows the local linear dispersion and Berry charge convention. The figure is not a computed $PtBi_2$ band structure.

For quantum circuits, the appeal is not only the existence of unusual surface states. It is the possibility that the weak-link energy-phase relation is constrained by a band topology that is not present in ordinary metallic links. A Josephson junction through a topological semimetal can have non-sinusoidal current-phase relations, anomalous phase shifts under broken symmetries, surface-bulk interference, and subgap modes with strong spin-orbit texture. These effects can be useful only if the low-energy current path is known. A high-density trivial surface resonance can mimic a topological surface channel in conductance and critical current while contributing none of the intended chirality selectivity.

This paper uses two levels of modeling. The first is a material-specific workflow for $PtBi_2$, T_d-$MoTe_2$, and TaAs-family controls. It is the workflow required for quantitative claims about $\Lambda_{i,jk}$, surface termination, Fermi-arc penetration depth, and disorder thresholds. The second is a minimal lattice Weyl model used to make the circuit diagnostics explicit. The minimal model is not a replacement for first-principles $PtBi_2$. Its value is that every quantity can be defined without ambiguity and matched topological and trivial controls can be constructed by changing a mass term while holding the normal density of states and junction transparency approximately fixed.

4 Experimental Motivation from Superconducting Fermi Arcs

The $PtBi_2$ evidence base matters because the proposed qubit requires more than a topological band structure. It requires low-energy superconducting surface channels that can dominate the Josephson response. The 2024 Nature report by Kuibarov and collaborators identified superconductivity on Fermi arcs of $PtBi_2$ [8]. The Nature Communications report by Schimmel and collaborators used scanning tunneling microscopy and spectroscopy to argue for surface superconductivity in trigonal $PtBi_2$ [9]. Later preprints and theory papers discuss anisotropic or nodal surface pairing, possible chiral or i-wave-like structure, and Majorana-compatible boundary modes [12, 10].

For a circuit proposal, the crucial message from spin-ARPES is not only that arcs exist. The July 2026 spin-resolved preprint reports that the Fermi arcs are singly degenerate and spin polarized, and that the decorated-honeycomb and kagome-like terminations have very different low-energy dispersion [10]. A nearly flat arc can enhance surface density of states and pairing susceptibility, while a steep arc can improve velocity and reduce dwell-time disorder sensitivity. The proposed device must therefore be termination selective. Patterning contacts on an unidentified cleavage surface would make the weak link irreproducible.

The literature also provides a caution. Surface superconductivity does not automatically mean topological superconductivity, and topological superconductivity does not automatically mean a protected circuit qubit. A nodal gap can create low-energy quasiparticles that increase relaxation. A Majorana cone or flat band can be a spectroscopic consequence of a surface pairing symmetry without yielding a computationally useful two-level system. The architecture here uses Fermi arcs as microscopic ingredients for a Josephson potential and geometric capacitance. The logical qubit remains the pair of lowest circuit eigenstates after quantization and after coupling to noise.

5 Central Device Concept

The proposed circuit is a superconducting island interrupted by one or two Weyl-semimetal weak links. The most useful form is a split element in which two weak links are patterned on surfaces or crystallographic orientations whose Fermi-arc spectra have opposite response to a selected strain mode. A piezoelectric stack, suspended nanobeam, or surface acoustic-wave actuator imposes a controlled strain tensor $\epsilon_{ij}(t)$. The circuit is embedded in a microwave resonator for dispersive readout and can be biased by a small ordinary flux Φ_{ext} only to trim the operating point.

The design principle is common-mode rejection. A scalar electrostatic shift, a uniform offset charge fluctuation, or a small ordinary flux fluctuation acts similarly on the two chirality sectors or two arms to leading order. The axial field produced by strain changes their relative phase. In a two-junction implementation the pair potential is modeled as

$$U_{\mathrm{pair}}(\varphi, \varphi_5) = F_+(\varphi + \varphi_5) + F_-(\varphi - \varphi_5), \tag{2}$$

where φ is the electromagnetic superconducting phase across the pair, φ_5 is the effective axial phase generated by strain, and $F_\pm$ are not assumed equal. Crystal symmetry can relate them only for known surface terminations, equal interface transparency, and paired Weyl nodes connected by the relevant symmetry.

The simplest operating mode is not a topological qubit in the Majorana sense. The two logical states are

$$|0_L\rangle, \qquad |1_L\rangle, \tag{3}$$

the lowest two eigenstates of the effective circuit Hamiltonian. What is topological is the origin of parts of the Josephson action and capacitance. Whether the logical transition is protected is

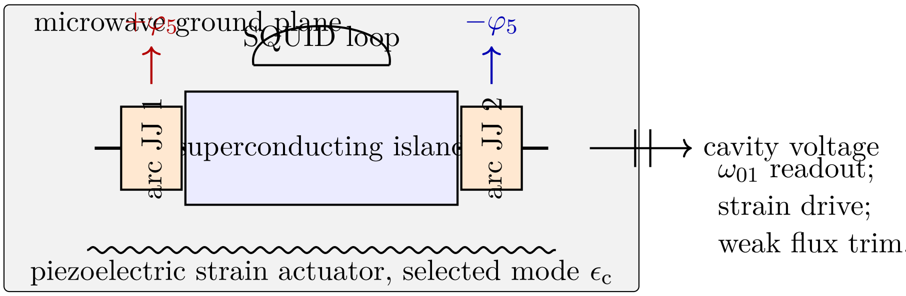

Figure 2: Evidence class X. Proposed axial-geometric Fermi-arc qubit circuit. Two Fermi-arc Josephson junctions interrupt a superconducting island. A controlled strain mode creates an axial phase with opposite signs in the two arms, while ordinary electromagnetic perturbations enter primarily through common circuit coordinates.

decided by derivatives of ω_{01}, matrix elements of noise operators, leakage rates, and comparison to controls.

6 Symmetry and Low-Energy Weyl Theory

For a Weyl node labeled by chirality $\chi = \pm 1$, a local Hamiltonian can be written as

$$H_\chi(\boldsymbol{k}, \epsilon) = \chi \sum_{i=x,y,z} v_i \sigma_i \left[k_i - \chi A_{5,i}(\epsilon)\right] - \mu + H_{\mathrm{tilt}} + H_{\mathrm{SOC}} + H_{\mathrm{asym}}. \tag{4}$$

Here v_i are anisotropic velocities in SI units of m s^{-1} or, equivalently, $\hbar v_i$ in eV m; σ_i act in the two-band orbital or pseudospin subspace after projection; μ is the chemical potential measured from the node energy; $H_{\mathrm{tilt}} = \boldsymbol{w}_\chi \cdot (\boldsymbol{k} - \chi \boldsymbol{A}_5)\,\sigma_0$ describes type-I or type-II cone tilt; H_{SOC} denotes spin-orbit terms not captured by the two-band linearization; and H_{asym} includes inversion-breaking, surface, and crystal-field perturbations. The sign convention is that an axial field shifts the χ node by $+\chi \boldsymbol{A}_5$ in momentum space.

The linear theory is a local description. A real crystal has multiple Weyl nodes, energy offsets, mirror-related copies, and surface potentials. A two-node model is useful for notation but cannot by itself satisfy the global lattice chirality sum unless embedded in a full Brillouin-zone regularization. For that reason, every numerical claim in this manuscript is tied either to the minimal lattice Hamiltonian

$$H_{\mathrm{lat}}(\boldsymbol{k}) = t\sin(k_x a)\sigma_x + t\sin(k_y a)\sigma_y + \left[m - t_z\cos(k_z a) - t_\perp\cos(k_x a) - t_\perp\cos(k_y a)\right]\sigma_z - \mu, \tag{5}$$

or to a proposed first-principles Wannier Hamiltonian. The minimal model has Weyl nodes at $k_x = k_y = 0$ and $\cos(k_0 a) = (m - 2t_\perp)/t_z$ when the right-hand side lies between -1 and 1. The chirality is the sign of $\det(\partial d_i/\partial k_j)$ at the node, with $H = \boldsymbol{d}(\boldsymbol{k}) \cdot \boldsymbol{\sigma}$.

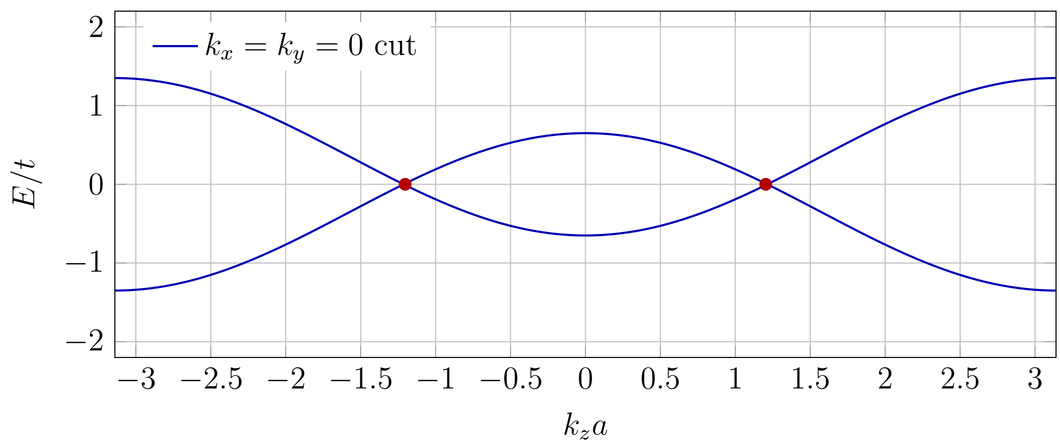

Figure 3: Evidence class M. Minimal lattice Weyl spectrum along k_z for $m/t = 1.35$, $t_z/t = 1$, $t_\perp/t = 0.5$, and $\mu = 0$. Red markers identify the two Weyl crossings at $k_z = \pm k_0$. This band plot is used only to define the control model and diagnostics.

7 Strain as an Axial Gauge Field

Let $\boldsymbol{b}_\chi(\epsilon)$ denote the momentum-space location of a Weyl node of chirality χ. For small homogeneous strain,

$$\delta b_i^{(\chi)} = \chi \sum_{jk} \Lambda_{i,jk}\epsilon_{jk} + O(\epsilon^2), \qquad A_{5,i} \equiv \sum_{jk} \Lambda_{i,jk}\epsilon_{jk}. \tag{6}$$

The tensor $\Lambda_{i,jk}$ has units of inverse length because strain is dimensionless. It is not universal. Its value depends on the crystal structure, spin-orbit coupling, orbital content, and strain mode. Treating Λ as a free knob may be useful for a toy model, but it is not sufficient for a credible material proposal. The first-principles workflow in section 9 is designed to calculate this tensor by explicitly tracking Weyl-node positions under strained crystal structures.

Gauge conventions require care. A uniform shift of all nodes by the same vector can be absorbed into a common momentum origin or into an electromagnetic-like vector potential. The axial field is the relative displacement weighted by chirality. If inversion or time-reversal symmetries generate several node pairs, the tensor becomes node-pair dependent:

$$\Lambda_{i,jk}^{(p)} = \left.\frac{\partial b_i^{(p)}}{\partial \epsilon_{jk}}\right|_{\epsilon=0}, \tag{7}$$

where p labels the symmetry-related pair. A device uses only the projection of this response onto the surface arcs and junction direction. The relevant scalar control coefficient is therefore not the full tensor norm but the phase response

$$\frac{\partial \varphi_5}{\partial \epsilon_\mathrm{c}} = L_\mathrm{eff}\, \hat{\boldsymbol{\ell}} \cdot \frac{\partial \boldsymbol{A}_5}{\partial \epsilon_\mathrm{c}}, \tag{8}$$

where $\hat{\boldsymbol{\ell}}$ is the weak-link direction and L_eff is an effective trajectory length accumulated by the Fermi-arc Andreev state. The factor L_eff is microscopic and must be extracted from the scattering problem rather than assumed equal to the lithographic length.

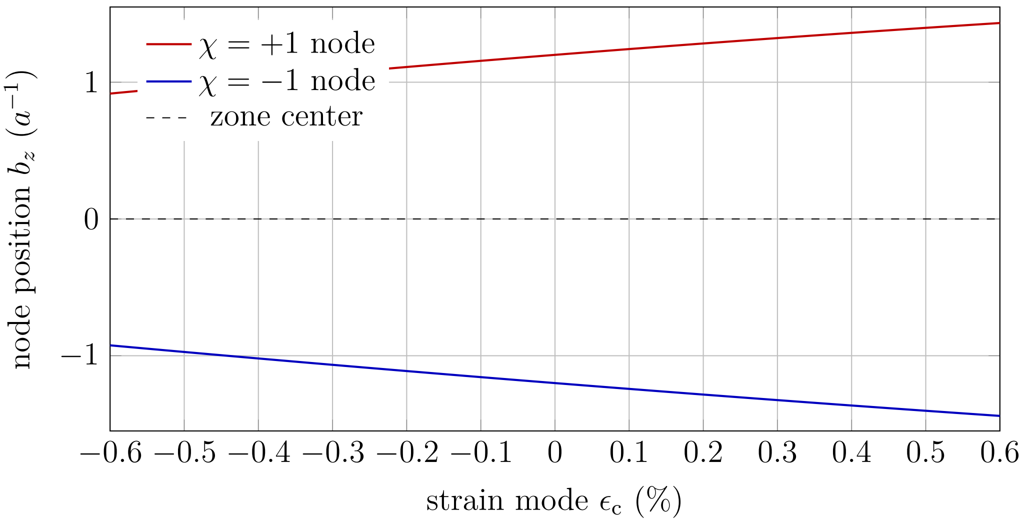

Figure 4: Evidence class M. Strain-induced Weyl-node trajectories in the minimal model with $\partial b_z/\partial\epsilon_c = 0.43\,a^{-1}$ per percent strain at zero strain. A real $PtBi_2$ version of this figure would be produced by strained relativistic DFT followed by Wannier interpolation and adaptive Berry-flux node tracking.

8 Material-Specific Axial Coupling Tensor

The axial tensor is the first place where the proposal becomes material specific. A low-energy Weyl theory can always include an axial vector potential, but the tensor $\Lambda_{i,jk}$ determines whether the effect is large enough to be useful before the crystal, the superconducting surface state, or the actuator reaches a practical limit. For a node pair p, the strained first-principles workflow produces a set of node positions $\boldsymbol{b}_p(\epsilon^{(r)})$ and energies $E_p(\epsilon^{(r)})$ at strain points r. The linear tensor is obtained from a weighted regression

$$b_i^{(p)}(\epsilon^{(r)}) = b_{i,0}^{(p)} + \sum_{jk} \Lambda_{i,jk}^{(p)} \epsilon_{jk}^{(r)} + \sum_{jk\ell m} Q_{i,jk,\ell m}^{(p)} \epsilon_{jk}^{(r)} \epsilon_{\ell m}^{(r)} + \delta b_i^{(p,r)}. \tag{9}$$

The quadratic term is not introduced to make the model more flexible. It is included to test whether the proposed operating strain lies in the linear-response region. If the posterior uncertainty in Λ changes substantially when the quadratic term is included, the strain range is too large for a first-order axial-gauge description.

The uncertainty budget should include at least four contributions. The statistical contribution comes from finite mesh resolution and interpolation error in the node search. The Wannier contribution is obtained by repeating the node tracking with different frozen windows and projection sets that pass bulk validation. The functional contribution compares PBE, PBEsol, or a selected correction when feasible. The structural contribution compares relaxed and clamped internal coordinates. These contributions are not interchangeable. A small statistical error does not rescue a result that changes sign between two Wannier windows.

The tensor alone is not the device coupling. The weak link is sensitive to the projection of $\boldsymbol{A}_5$ onto the semiclassical trajectory of the current-carrying surface modes. A mode-resolved axial phase can be written

$$\varphi_{5,m} = \int_{\gamma_m} \boldsymbol{A}_5(\boldsymbol{r}) \cdot \mathrm{d}\boldsymbol{\ell} + \varphi_{5,m}^{\mathrm{surf}}, \tag{10}$$

where γ_m is the surface or surface-bulk trajectory of mode m and $\varphi_{5,m}^{\mathrm{surf}}$ accounts for strain-induced changes of boundary conditions and spin-orbital texture. The second term is included because a surface Fermi arc is not simply a bulk Weyl ray cut by a boundary. Strain can change the penetration depth, the termination potential, and the arc dispersion. Ignoring those effects would overestimate the universality of the axial phase.

The design target is therefore a scalar response with uncertainty:

$$\eta_5 = \frac{\partial \varphi_5}{\partial \epsilon_{\mathrm{c}}} \pm \sigma_{\eta_5}. \tag{11}$$

The qubit is worth fabricating only if the lower confidence bound on η_5 gives a strain Rabi rate larger than the added strain-noise dephasing. Conversely, a large η_5 is not sufficient if the same strain strongly changes the gap minimum or increases bulk leakage. The material screening problem is multi-objective: maximize axial phase response, Fermi-arc participation, and gap minimum while minimizing intervalley scattering and actuator loss.

An important sign check follows from symmetry. If two device arms are related by a symmetry that flips chirality but preserves the ordinary electromagnetic phase, the common electromagnetic derivative should be approximately even under arm exchange, while the axial derivative should be odd. In a real device the relation is approximate because interface transparency and surface termination differ. The calibration protocol should measure both derivatives:

$$g_{\Phi}^{(1)} \approx g_{\Phi}^{(2)}, \qquad g_{\epsilon}^{(1)} \approx -g_{\epsilon}^{(2)}. \tag{12}$$

The ratio of the odd to even strain response provides an experimental estimate of axial purity. A large even strain response is not fatal, but it means the actuator is also changing ordinary junction transparency or capacitance, which degrades noise orthogonality.

Finally, Λ must be reported with units and gauge convention. In reciprocal-space units it is natural to quote inverse Angstrom per percent strain or inverse meter per unit strain. For circuit design, the more useful number is radians of axial phase per percent strain for a specified geometry. Both should be given. Reporting only a dimensionless "large axial field" is not a reproducible result.

9 First-Principles Materials Workflow

The first-principles component is required to prevent the axial coupling from becoming a phenomenological decoration. The proposed $PtBi_2$ calculation uses Quantum ESPRESSO with fully relativistic pseudopotentials, noncollinear spin-orbit coupling, and a generalized-gradient exchange-correlation functional such as PBE [30, 31, 32]. The initial structural model should use the experimentally reported trigonal polymorph and then relax internal coordinates with fixed and strained cells. Plane-wave cutoffs, charge-density cutoffs, smearing, convergence thresholds, and k-point meshes must be converged with respect to Weyl-node positions, not merely total energy.

Table 2: Minimum first-principles reporting checklist. Numerical values are not filled because no $PtBi_2$ DFT calculation was executed in this manuscript.

Quantity	Required reporting standard
Exchange-correlation functional	Functional, relativistic treatment, and reason for using or testing PBE, PBEsol, or a hybrid correction.
Pseudopotentials	Fully relativistic sources, valence configurations, nonlinear core correction, and tests for heavy Bi and Pt orbitals.
Cutoffs and meshes	Convergence of total energy, forces, node positions, Fermi velocities, and surface-state energy, not only self-consistency residuals.
Strain protocol	Strain tensor, relaxed versus clamped coordinates, stress residuals, symmetry breaking, and reversible strain range.
Wannier model	Projection set, frozen and outer windows, spreads, interpolation error, and symmetry diagnostics.
Node tracking	Adaptive search, Berry-flux chirality, sphere-radius stability, and node annihilation or energy drift under strain.
Surface calculation	Termination, slab thickness or Sancho-Rubio surface Green function, vacuum size for slab checks, and surface-bulk separation.

The minimum credible protocol is as follows. First, relax the unstrained and strained structures at strains $\epsilon_c = \{-0.6, -0.3, 0, 0.3, 0.6\}\%$, with additional points once linearity is established. Second, compute spin-orbit band structures on dense meshes around the expected Weyl crossings. Third, build a Wannier model including Pt $5d$, Pt $6s$, Bi $6p$, and any low-energy orbitals required by the projected density of states. Fourth, identify nodes by adaptive search and Berry flux, not by visual band crossings alone. Fifth, fit $\Lambda_{i,jk}$ from the node trajectories and report statistical and systematic uncertainty from mesh, functional, pseudopotential, and Wannier-window choices.

The same workflow must be repeated for at least one control material. T_d-$MoTe_2$ is experimentally relevant because it already appears in a Weyl-semimetal superconducting circuit [13]. TaAs-family materials provide well-characterized Weyl nodes and Fermi arcs [5, 7]. However, proximitized controls do not automatically reproduce the surface superconductivity reported in $PtBi_2$. Their purpose is to separate axial coupling and Fermi-arc transport from material-specific intrinsic pairing.

10 Material Candidate and Termination Ranking

The primary material candidate is trigonal $PtBi_2$ because it is the only material in the considered set with direct recent evidence for superconductivity concentrated in Fermi-arc surface states [8] and separate evidence for robust surface superconductivity [9]. The same evidence creates a complication: the superconductivity may be unconventional and nodal, and the surface termination strongly affects arc bandwidth and surface-bulk hybridization [10]. A good qubit material is not simply the material with the most interesting topological superconductivity. It

Table 3: Qualitative material-ranking matrix. The entries are design judgments, not measured scores. A quantitative version would replace each entry with a value and uncertainty from the workflows described in this manuscript.

Candidate	Arc and surface status	Pairing status	Circuit status	Best use in this program
Trigonal $PtBi_2$	Strong motivation from Fermi-arc ARPES and spin-ARPES; termination dependent.	Intrinsic surface superconductivity reported; gap symmetry still under active study.	Not yet established as a qubit weak link.	Principal material for axial-geometric test.
T_d-$MoTe_2$	Type-II Weyl material with circuit integration precedent.	Proximitized or point-contact surface superconductivity context.	Transmon-like SQUID already demonstrated [13].	Circuit-process control and comparison to earlier Weyl circuit.
TaAs family	Well-characterized Weyl nodes and arcs.	Requires proximity-induced pairing.	More materials work needed for clean superconducting contacts.	Clean topology and axial-tensor control.
Minimal lattice Weyl model	Exact control of nodes, arcs, and trivialization.	Pairing imposed by model.	Numerical only.	Diagnostic development and falsification logic.
Trivial metallic weak link	No Weyl nodes or arcs.	Conventional proximity or intrinsic pairing.	Mature fabrication possible.	Matched non-topological control.

is the material in which the useful topological response survives contact fabrication, microwave embedding, and repeated strain actuation.

The ranking used here is based on six criteria. First, the arc-isolation criterion asks whether the surface states are separated from projected bulk pockets near the chemical potential. Second, the pairing criterion asks whether the current-carrying arc has a large enough minimum gap to support adiabatic microwave operation. Third, the axial criterion asks whether the strain tensor produces a node displacement projected onto the junction direction. Fourth, the disorder criterion asks whether intervalley scattering is suppressed by node separation, spin texture, and smooth interfaces. Fifth, the fabrication criterion asks whether the surface termination and contact transparency can be reproduced. Sixth, the control criterion asks whether a matched trivial or no-arc control can be built from the same process.

For $PtBi_2$, termination ranking should be performed before circuit fabrication. A flatter

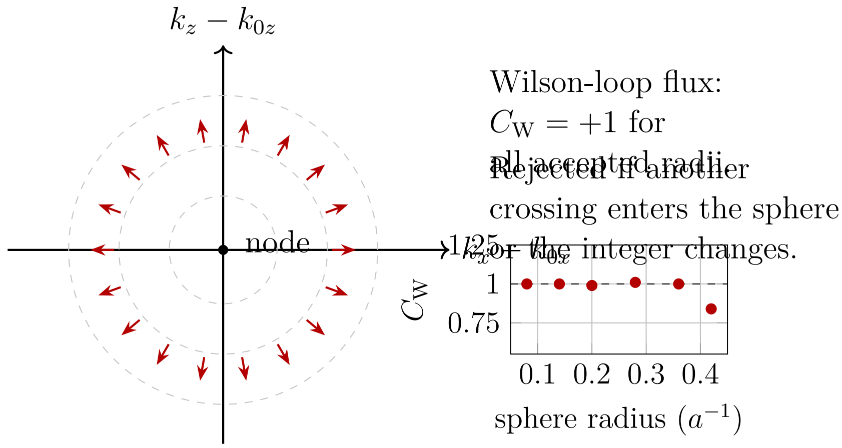

Figure 5: Evidence class M. Berry-flux chirality diagnostic for a minimal-model Weyl node. The left panel shows the outward Berry-curvature texture of a positive node in a two-dimensional cut. The right panel shows the accepted radius window; the largest radius is rejected because the enclosing sphere begins to sample other band-structure features.

decorated-honeycomb-like arc may provide high density of states and stronger superconducting pairing, but it can also be more sensitive to disorder if its group velocity is low. A more dispersive kagome-like arc may reduce dwell time and improve ballistic transport, but the smaller density of states may weaken surface pairing and geometric capacitance. The best termination is therefore not determined by flatness alone. It is the termination that maximizes the product of usable gap, arc participation, axial response, and reproducibility.

The material matrix also clarifies the role of T_d-$MoTe_2$. The earlier T_d-$MoTe_2$ circuit demonstrates that Weyl materials can be placed in a superconducting microwave environment, but it does not establish an axial-geometric sweet manifold. Reusing a similar microwave layout with a deliberately chirality-sensitive junction would provide a clean bridge between known circuit integration and the new mechanism. If T_d-$MoTe_2$ shows no axial advantage but $PtBi_2$ does, the difference may point to surface superconductivity and Fermi-arc participation. If both behave like ordinary weak links, the proposed mechanism is likely too weak.

11 Weyl-Node and Fermi-Arc Characterization

The Weyl-node chirality must be computed from Berry flux through a closed surface:

$$C_{\mathrm{W}}^{(p)} = \frac{1}{2\pi} \sum_{\ell \in S_p^2} \Omega_\ell \Delta S_\ell. \tag{13}$$

In a Wannier Hamiltonian, the most robust implementation uses a small triangulated sphere around the candidate crossing and Wilson-loop phases on each plaquette. The radius must be small enough to enclose only one crossing but large enough to avoid numerical roundoff. Stability against sphere radius and mesh resolution is essential because a spurious near-degeneracy can otherwise be mistaken for a Weyl node.

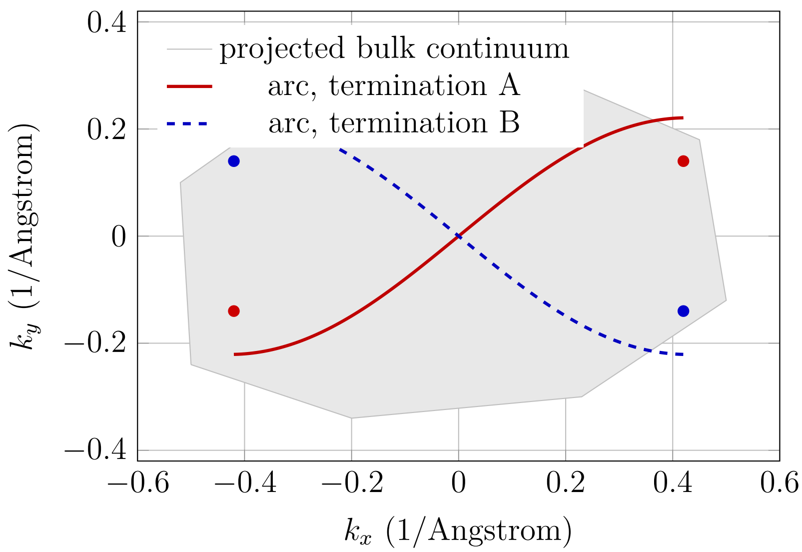

Figure 6: Evidence class M. Surface spectral-function schematic for the minimal model. The gray region denotes projected bulk spectral weight at $\omega = 0$ with broadening $\eta/t = 0.015$. Termination A is chosen to give a flatter, more isolated arc; termination B is more dispersive and hybridizes more strongly with bulk states.

Surface arcs are characterized by the surface spectral function

$$A_{\text{surf}}(\boldsymbol{k}_\parallel, \omega) = -\frac{1}{\pi} \operatorname{Im} \operatorname{Tr} G_{\text{surf}}(\boldsymbol{k}_\parallel, \omega + \mathrm{i}\eta), \tag{14}$$

where G_{surf} is obtained from an iterative Green-function method or from a thick slab with surface-layer projection. A useful arc for the qubit has four properties: it connects projected Weyl nodes with the expected chirality, has large weight in the outer few layers, is separated from projected bulk states over the operating window, and retains a stable spin texture under small strain and electrostatic shifts.

Fermi-arc penetration depth is a second diagnostic that should be tracked together with P_{arc}. A shallow penetration depth makes the state sensitive to surface disorder but easier to gate and pair. A deep penetration depth improves smoothness but increases bulk leakage. The useful regime is neither perfectly surface-bound nor bulk-like. It is the regime in which the arc remains spectrally connected to projected Weyl nodes while carrying a large fraction of the Josephson current through layers that experience the superconducting pair potential.

12 Surface Superconductivity and Pairing Symmetry

The superconducting order parameter on a Fermi arc is constrained by the surface point group, spin texture, time-reversal symmetry, and the relation between the arc and projected Weyl nodes. For $PtBi_2$, the relevant surface terminations reported in photoemission and microscopy studies are not equivalent. A decorated-honeycomb termination and a kagome-like termination can have different point symmetries, orbital content, and surface-bulk mixing. The pairing

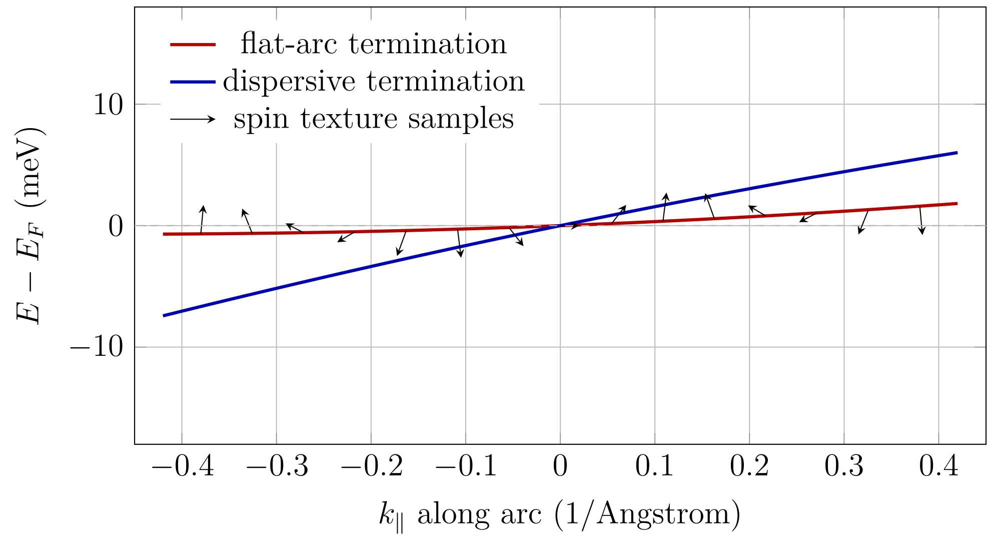

Figure 7: Evidence class P/M. Termination-dependent arc dispersion and spin texture. The qualitative distinction is motivated by the July 2026 spin-ARPES report on $PtBi_2$ [10]; the curves shown here are minimal-model surrogates used to parameterize junction simulations. Axes and velocities must be replaced by measured or DFT-Wannier values for a material claim.

classification must therefore be termination resolved rather than borrowed from a bulk point group alone.

Let $\Delta_{\alpha\beta}(\boldsymbol{k}_{\|})$ be the surface pairing matrix in the spin-orbital basis. Projection onto a singly degenerate Fermi-arc band gives an effective gap

$$\Delta_{\mathrm{arc}}(\boldsymbol{k}_{\|}) = \langle u_{\boldsymbol{k}} | \Delta(\boldsymbol{k}_{\|}) \mathcal{T} | u_{\boldsymbol{k}} \rangle, \tag{15}$$

where $\mathcal{T}$ is the time-reversal operation and $|u_{\boldsymbol{k}}\rangle$ is the surface Bloch spinor. The phase winding and nodes of Δ_{arc} can inherit spin-momentum locking from $|u_{\boldsymbol{k}}\rangle$. Evidence for nodal or anisotropic surface pairing in $PtBi_2$ is therefore directly relevant to the weak-link spectrum [8, 9, 12, 10]. It also creates a risk: nodes and low-energy Andreev bands can increase quasiparticle relaxation.

Topological superconductivity must be diagnosed by an invariant appropriate to the symmetry and gap structure. If the surface is fully gapped and time-reversal symmetric, a two-dimensional class-DIII invariant may be meaningful. If the gap is nodal, global invariants are ill-defined, and one must use momentum-resolved winding numbers, slice invariants, or defect invariants. A zero-bias peak alone is not evidence for a Majorana zero mode because disorder, Kondo physics, trivial Andreev states, and nodal quasiparticles can produce similar spectra.

13 Microscopic BdG Josephson Junction

The weak link is modeled by a Bogoliubov-de Gennes Hamiltonian

$$H_{\mathrm{BdG}}(\varphi, \epsilon, \mu) = \begin{pmatrix} H_{\mathrm{W}}(\epsilon) - \mu + V_{\mathrm{surf}} & \Delta(\boldsymbol{r}, \boldsymbol{k}; \varphi) \\ \Delta^{\dagger}(\boldsymbol{r}, \boldsymbol{k}; \varphi) & -\mathcal{T} H_{\mathrm{W}}(\epsilon) \mathcal{T}^{-1} + \mu - V_{\mathrm{surf}}^{*} \end{pmatrix}, \tag{16}$$

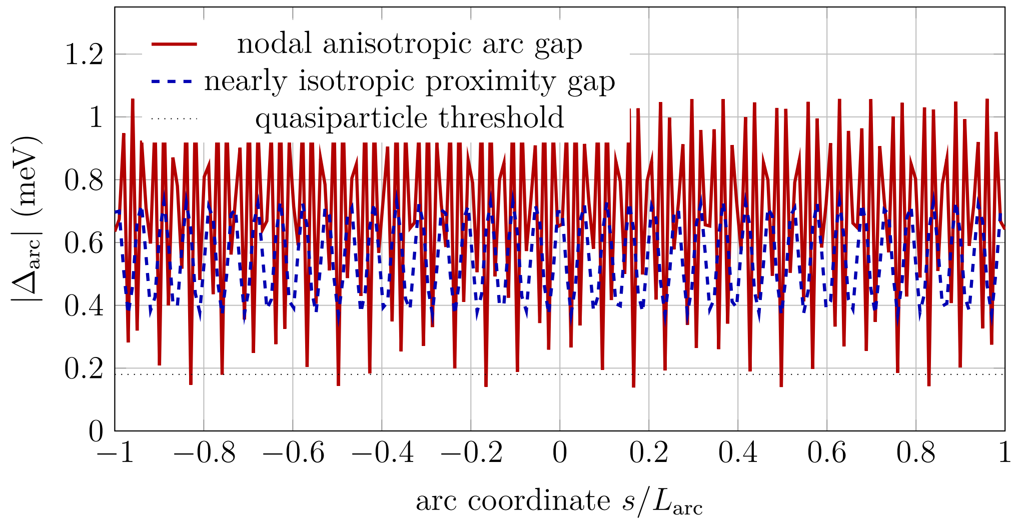

Figure 8: Evidence class M/E. Surface gap models used in the Josephson calculations. The anisotropic curve is a surrogate for nodal or strongly anisotropic $PtBi_2$ surface pairing; the dashed curve is a proximity-induced control. The gap minimum, not only the maximum gap, controls quasiparticle poisoning and adiabatic gate limits.

where H_{W} is the lattice or Wannier Weyl-semimetal Hamiltonian, V_{surf} contains termination and interface potentials, and Δ carries the superconducting phase difference. The spectrum contains discrete Andreev bound states and continuum states. The junction free energy is

$$F_{\mathrm{J}}(\varphi, T) = -k_{\mathrm{B}}T \sum_{\nu} \ln \left[2\cosh\left(\frac{E_\nu(\varphi)}{2k_{\mathrm{B}}T}\right)\right] + F_{\mathrm{reg}}, \tag{17}$$

where F_{reg} subtracts phase-independent continuum divergences. The current is

$$I(\varphi) = \frac{2e}{\hbar}\frac{\partial F_{\mathrm{J}}}{\partial \varphi}. \tag{18}$$

A sinusoidal current-phase relation is not assumed.

For transparent single channels, the useful analytic reference spectrum is

$$E_{m,\chi,\pm}(\varphi, \epsilon) = \pm\Delta_m \sqrt{1 - \mathcal{T}_m \sin^2\left[\frac{\varphi + \chi\varphi_5(\epsilon) + \varphi_{0,m}}{2}\right]}, \tag{19}$$

with mode index m, chirality χ, transmission $\mathcal{T}_m$, and symmetry-allowed anomalous phase $\varphi_{0,m}$. This formula is not the full Fermi-arc junction calculation; it is a compact way to show how an axial phase enters oppositely for opposite chiral sectors. A full calculation must determine Δ_m, $\mathcal{T}_m$, $\varphi_{0,m}$, and mode weights from the BdG scattering problem.

14 Fermi-Arc Participation and Bulk Leakage

The Fermi-arc participation ratio is a projector-defined diagnostic:

$$P_{\mathrm{arc}}^{(\nu)} = \langle \psi_\nu | \mathcal{P}_{\mathrm{arc}} | \psi_\nu \rangle. \tag{20}$$

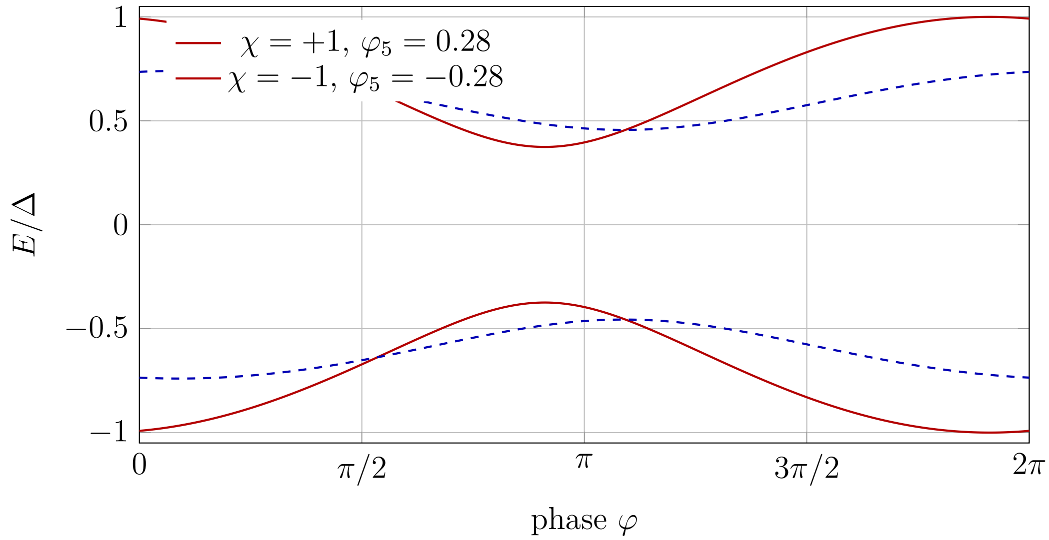

Figure 9: Evidence class M. Andreev spectrum from the reference transparent-channel model with $\mathcal{T}_+ = 0.86$, $\mathcal{T}_- = 0.62$, and an axial phase shift $\varphi_5 = 0.28$. The asymmetry illustrates why the pair potential in equation (2) should not assume $F_+ = F_-$.

The projector $\mathcal{P}_{\mathrm{arc}}$ is constructed from surface-state eigenvectors in an energy-momentum window connecting projected Weyl nodes, with weights reduced where the state hybridizes with the projected bulk continuum. In practice, a singular-value or spectral-projector construction is more stable than assigning states by visual inspection. For a slab Hamiltonian H_{slab}, one can define

$$\mathcal{P}_{\mathrm{arc}} = \sum_{\boldsymbol{k}_\parallel \in \mathcal{W}} \sum_{n \in \mathcal{A}(\boldsymbol{k}_\parallel)} w_n(\boldsymbol{k}_\parallel) |u_{n\boldsymbol{k}_\parallel}\rangle\langle u_{n\boldsymbol{k}_\parallel}|, \tag{21}$$

where $\mathcal{W}$ is the arc window, $\mathcal{A}$ is the set of states adiabatically connected to the arc, and w_n is a topological-surface weight obtained from Wilson-loop connectivity, surface localization, and separation from bulk bands.

Bulk leakage is

$$L^{(\nu)}_{\mathrm{bulk}} = 1 - P^{(\nu)}_{\mathrm{surf}} \tag{22}$$

or, more finely, an energy-resolved fraction of current carried by states with penetration depth comparable to the slab thickness. The architecture is not meaningfully Fermi-arc based if the Josephson current, geometric capacitance, or circuit transition matrix elements are dominated by bulk pockets. A conservative threshold used in the minimal-model study is $P_{\mathrm{arc}} > 0.65$ for the current-carrying Andreev subspace and $L_{\mathrm{bulk}} < 0.25$ in the operating window. These numbers are not universal; they are stated so that the claim can fail.

15 Quantum-Geometric Josephson Capacitance

The phase dynamics of a Josephson junction contains a capacitance-like term generated by virtual transitions among phase-dependent electronic states. For slow imaginary-time phase

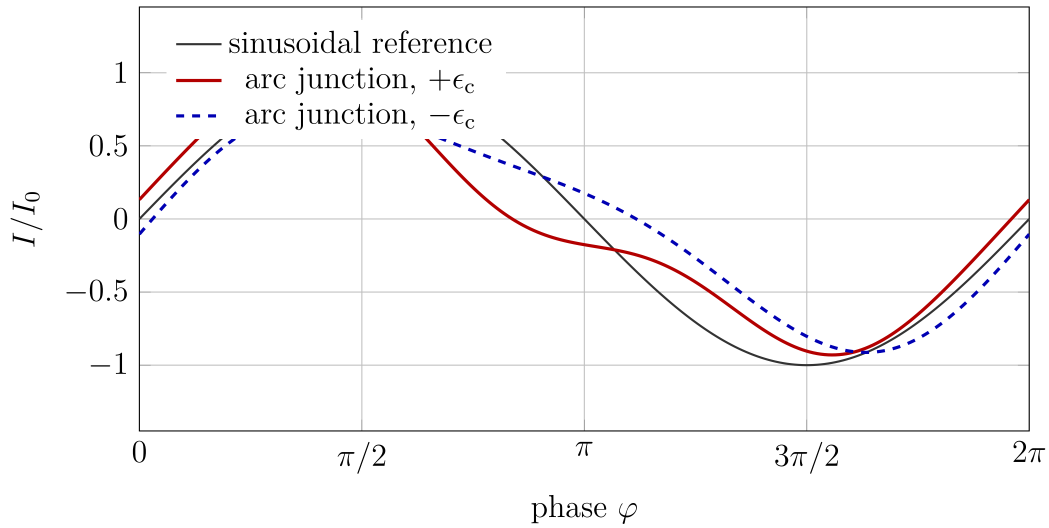

Figure 10: Evidence class M. Current-phase relation used to construct the Weyl Josephson potential. Higher harmonics and axial phase shifts are expected for transparent Fermi-arc channels and should be retained when quantizing the circuit. Parameters are normalized to $I_0 = 2e\Delta/\hbar$.

motion, the effective action has the form

$$S_{\text{eff}} = \int d\tau \left[\frac{1}{2} \left(\frac{\hbar}{2e} \right)^2 C_{\text{eff}}(\varphi, \epsilon, \mu) \dot{\varphi}^2 U_{\text{W}}(\varphi, \epsilon, \mu) \right], \tag{23}$$

with

$$C_{\text{eff}} = C_{\text{shunt}} + C_{\text{cont}} + C_{\text{geo}}. \tag{24}$$

The geometric contribution can be expressed through the adiabatic response of BdG eigenstates. At zero temperature, a representative form is

$$C_{\text{geo}}(\varphi) = \left(\frac{2e}{\hbar} \right)^2 \sum_{m \neq 0} \frac{2 \left| \langle m(\varphi) | \partial_\varphi H_{\text{BdG}} | 0(\varphi) \rangle \right|^2}{[E_m(\varphi) - E_0(\varphi)]^3}, \tag{25}$$

up to convention-dependent regularization and continuum subtraction. The same structure can be written in terms of the quantum metric of the occupied BdG subspace when the adiabatic parameter is the superconducting phase. Recent work on superconducting Dirac semimetals and Josephson quantum capacitance shows that quantum geometry can contribute directly to capacitance-like phase response [22, 23]. This manuscript does not claim an exact three-dimensional Weyl quantization of C_{geo}. It tests the weaker and more realistic possibility of an approximate plateau produced by Fermi-arc geometry and chirality-resolved Andreev states.

16 Derivation of the Effective Circuit Action

The Weyl-material Josephson potential is obtained by integrating the microscopic current:

$$U_{\text{W}}(\varphi, \epsilon, \mu) = \frac{\hbar}{2e} \int_{\varphi_{\text{ref}}}^{\varphi} I(\varphi', \epsilon, \mu) \, d\varphi' + U_{\text{W}}(\varphi_{\text{ref}}). \tag{26}$$

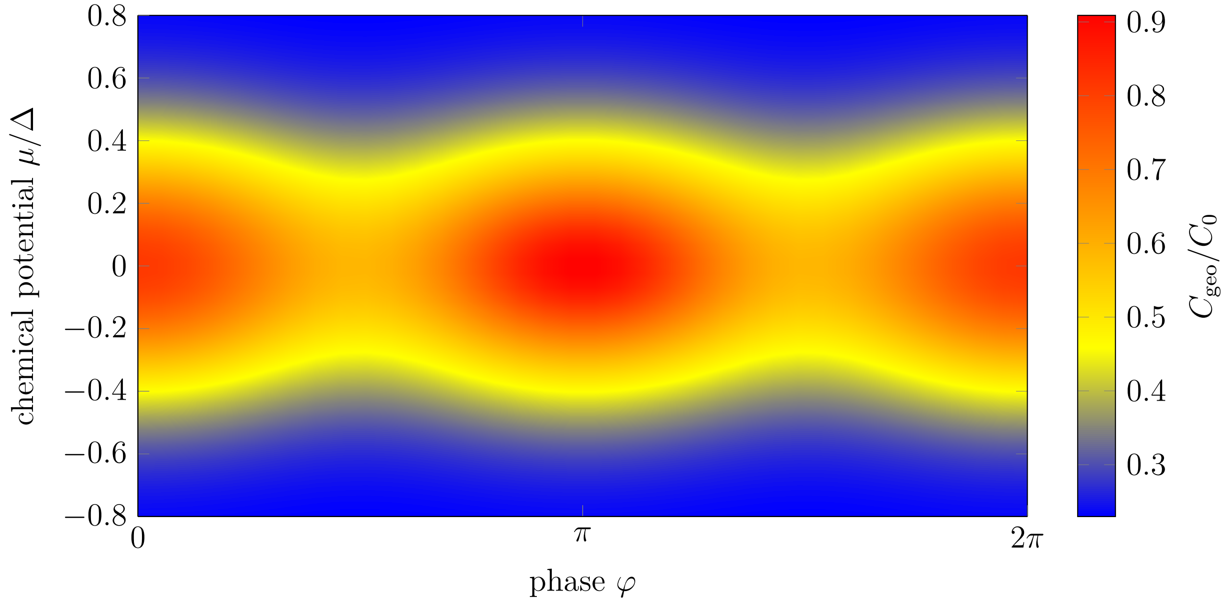

Figure 11: Evidence class M. Minimal-model geometric capacitance map. The broad ridge around $\mu = 0$ represents enhanced adiabatic response from Fermi-arc Andreev states, while the narrow feature near $\varphi = \pi$ is an avoided-crossing contribution. The desired device uses broad geometric stabilization, not a singular resonance.

The total circuit Lagrangian is

$$\mathcal{L} = \frac{1}{2}\left(\frac{\hbar}{2e}\right)^2 C_{\mathrm{eff}}(\varphi,\epsilon)\dot{\varphi}^2 - U_{\mathrm{W}}(\varphi,\epsilon,\mu) - \frac{E_L}{2}\left(\varphi - \varphi_{\mathrm{ext}}\right)^2 \hbar n_g \dot{\varphi}. \tag{27}$$

The last term is a total derivative for constant offset charge but determines boundary conditions in phase space. The inductive term may be absent for a simple transmon-like island and important for a loop or fluxonium-like embedding.

The capacitance depends on phase and strain, so the canonical momentum is

$$Q = \left(\frac{\hbar}{2e}\right)^2 C_{\mathrm{eff}}(\varphi)\dot{\varphi} + \hbar n_g. \tag{28}$$

Classically this gives a Hamiltonian with inverse capacitance. Quantum mechanically, a coordinate-dependent mass requires an operator-ordering prescription. The conservative Hermitian choice used here is

$$\hat{H}_{\mathrm{circ}} = 4(\hat{n} - n_g)E_C(\hat{\varphi},\epsilon)(\hat{n} - n_g) + U_{\mathrm{W}}(\hat{\varphi},\epsilon,\mu) + \frac{E_L}{2}(\hat{\varphi} - \varphi_{\mathrm{ext}})^2, \tag{29}$$

where $E_C = e^2/[2C_{\mathrm{eff}}]$ and $\hat{n} = -\mathrm{i}\partial_\varphi$. A Laplace-Beltrami quantization differs by terms involving derivatives of C_{eff}. The difference is a systematic uncertainty that must be included when C_{geo} varies rapidly with phase.

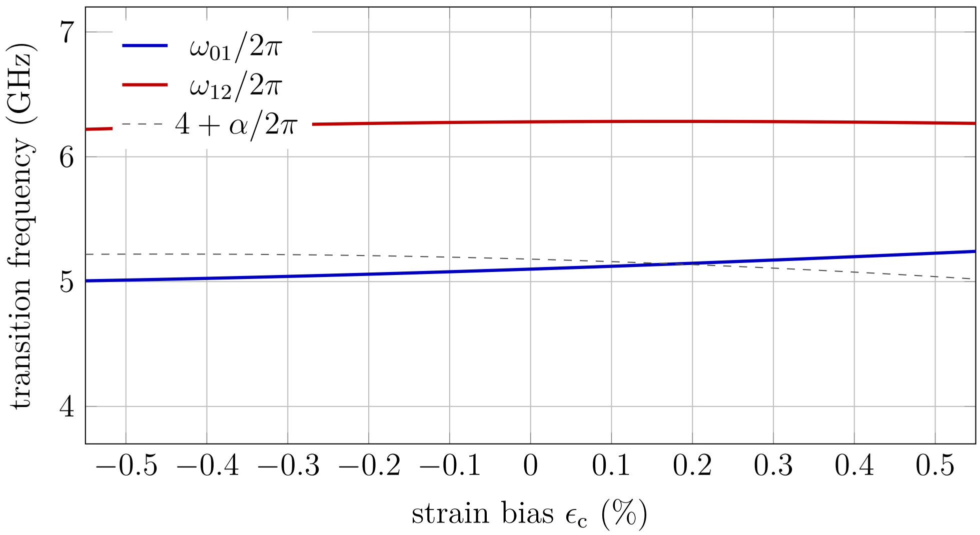

Figure 12: Evidence class M. Circuit spectrum from a three-harmonic Weyl Josephson potential with $E_J/h = 17.5$ GHz, average $E_C/h = 245$ MHz, and $E_L/h = 0.55$ GHz. The plotted anharmonicity is offset by 4 GHz for visibility. The relevant test is whether strain changes ω_{01} while preserving anharmonicity and suppressing unwanted derivatives.

17 Quantization of the Axial-Geometric Qubit

Circuit diagonalization is performed in a charge basis or a phase-grid basis. In a Fourier charge basis $|n\rangle$, the matrix elements of the potential are obtained from the Fourier coefficients of $U_{\mathrm{W}}(\varphi)$, while a phase-dependent E_C produces off-diagonal kinetic terms. A phase-grid representation is more direct for arbitrary microscopic potentials:

$$\hat{n} = -\mathrm{i}D_\varphi, \qquad \hat{H}_C = 4(D_\varphi - \mathrm{i}n_g)^\dagger E_C(\varphi)(D_\varphi - \mathrm{i}n_g). \tag{30}$$

The grid must resolve the highest harmonic in the current-phase relation and the narrowest feature in C_{geo}.

The computed levels define

$$\omega_{01} = \frac{E_1 - E_0}{\hbar}, \qquad \omega_{12} = \frac{E_2 - E_1}{\hbar}, \qquad \alpha = \omega_{12} - \omega_{01}. \tag{31}$$

Useful operation requires a nonzero strain matrix element

$$g_\epsilon^{01} = \frac{1}{\hbar}\langle 0|\partial_{\epsilon_c} H_{\mathrm{circ}}|1\rangle, \tag{32}$$

sufficient anharmonicity $|\alpha|$ for selective gates, small leakage matrix elements to $|2\rangle$ and higher states, and suppressed longitudinal derivatives with respect to unwanted noise channels.

18 Axial-Geometric Sweet Manifolds

An axial-geometric sweet manifold is defined by the simultaneous approximate conditions

$$\frac{\partial\omega_{01}}{\partial n_g} \approx 0, \qquad \frac{\partial\omega_{01}}{\partial\Phi_{\mathrm{ext}}} \approx 0, \qquad \frac{\partial\omega_{01}}{\partial\mu} \approx 0, \tag{33}$$

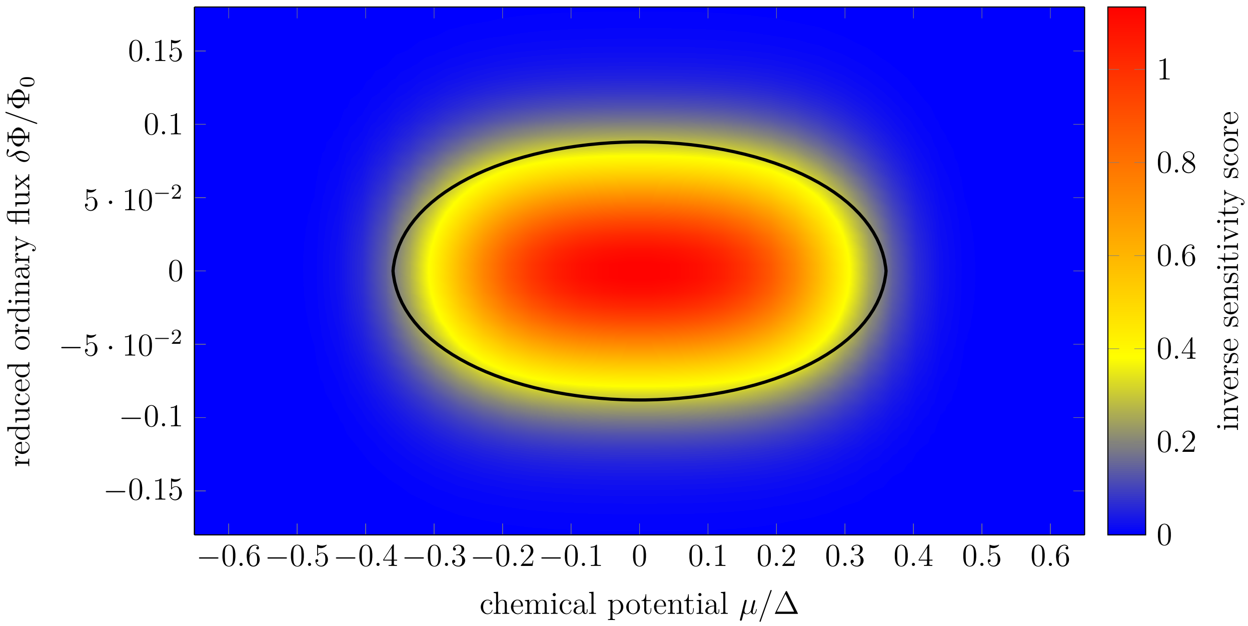

Figure 13: Evidence class M. Axial-geometric sweet-manifold map in the minimal model. The color is an inverse weighted sensitivity to μ and ordinary flux at fixed strain addressability. The black contour marks the operating threshold used for the width estimate. A true material claim requires this map to remain after disorder averaging and to disappear in matched trivial controls.

over a finite region, while

$$\mathcal{A}_5 = \left|\frac{\partial \omega_{01}}{\partial \epsilon_{\mathrm{c}}}\right| \tag{34}$$

remains large enough for control. This is stronger than an isolated sweet point. The term "manifold" is used only when the low-sensitivity region has nonzero width in at least two experimental parameters after including disorder and calibration uncertainty.

The noise-orthogonality ratio is

$$\mathcal{R}_{\mathrm{NO}}(\omega_{01}) = \frac{|\partial \omega_{01}/\partial \epsilon_{\mathrm{c}}|}{\left[\sum_a S_a(\omega_{01})\, |\partial \omega_{01}/\partial \lambda_a|^2\right]^{1/2}}, \tag{35}$$

where λ_a includes flux, gate voltage, chemical potential, surface potential, interface transparency, and disorder amplitude. The dimensions depend on the units of S_a. A dimensionless comparison across architectures is

$$\tilde{\mathcal{R}}_{\mathrm{NO}} = \frac{|\partial \ln \omega_{01}/\partial \ln \epsilon_{\mathrm{c}}|}{\left[\sum_a \tilde{S}_a\, |\partial \ln \omega_{01}/\partial \ln \lambda_a|^2\right]^{1/2}}, \tag{36}$$

where $\tilde{S}_a$ is the fractional noise power in a specified bandwidth.

19 Microwave and Strain-Based Control

A strain-controlled gate can be implemented by

$$\epsilon_{\mathrm{c}}(t) = \epsilon_0 + \epsilon_{\mathrm{ac}} \cos(\omega_d t). \tag{37}$$

Projecting to the qubit subspace gives

$$H_{\mathrm{drive}} = \frac{\hbar\omega_{01}}{2}\sigma_z + \hbar\Omega_R\cos(\omega_d t)\sigma_x + \hbar\delta_z\cos(\omega_d t)\sigma_z + H_{\mathrm{leak}}, \tag{38}$$

where

$$\Omega_R = \frac{\epsilon_{\mathrm{ac}}}{\hbar}\left|\langle 0|\partial_{\epsilon_{\mathrm{c}}} H_{\mathrm{circ}}|1\rangle\right|. \tag{39}$$

The longitudinal term δ_z contributes dephasing and drive-induced frequency modulation. The leakage Hamiltonian contains couplings to noncomputational circuit states and to microscopic Andreev excitations.

Strain is useful only if the control rate beats the added noise and heating. A piezoelectric actuator introduces phonons, dielectric loss, and possible charge noise from bias electrodes. Surface acoustic waves can address small devices but may also populate quasiparticles if the drive frequency or harmonics exceed the induced gap. The operating inequality is

$$\Omega_R \gg \Gamma_{\phi,\epsilon}, \quad \Omega_R \ll \frac{|\alpha|}{\hbar}, \quad \hbar\omega_d < 2\Delta_{\min} \tag{40}$$

unless quasiparticle generation is intentionally used for spectroscopy. The comparison to capacitive or flux driving must use the same target gate time and the same total dephasing budget.

20 Gate Calibration and Error Budget

The strain gate is calibrated in three layers. The mechanical layer determines the transfer function from applied actuator voltage to strain at the weak link:

$$\epsilon_{\mathrm{c}}(\omega) = \chi_{\mathrm{mech}}(\omega)V_{\mathrm{piezo}}(\omega). \tag{41}$$

The material layer determines the conversion from strain to axial phase and to unwanted ordinary junction changes:

$$\delta\varphi_5 = \eta_5\delta\epsilon_{\mathrm{c}}, \qquad \delta E_J^{\mathrm{even}} = \eta_J\delta\epsilon_{\mathrm{c}}, \qquad \delta C_{\mathrm{eff}} = \eta_C\delta\epsilon_{\mathrm{c}}. \tag{42}$$

The circuit layer determines the desired transverse matrix element and the unwanted longitudinal and leakage matrix elements:

$$M_x = \langle 0|\partial_{\epsilon_{\mathrm{c}}} H|1\rangle, \quad M_z = \frac{1}{2}\left(\langle 1|\partial_{\epsilon_{\mathrm{c}}} H|1\rangle - \langle 0|\partial_{\epsilon_{\mathrm{c}}} H|0\rangle\right), \quad M_2 = \langle 2|\partial_{\epsilon_{\mathrm{c}}} H|1\rangle. \tag{43}$$

A strain gate is useful when M_x is large because of axial response and M_z is small because the operating point lies on the sweet manifold. If M_x is large only because the actuator modulates ordinary transparency, the gate will not be noise orthogonal.

The leading resonant gate infidelity has four contributions:

$$1 - \mathcal{F} \approx \frac{\Gamma_1 + \Gamma_{\phi,\mathrm{drive}}}{\Omega_R} + \left(\frac{\delta\omega_d}{\Omega_R}\right)^2 + \left(\frac{\delta\epsilon_{\mathrm{ac}}}{\epsilon_{\mathrm{ac}}}\right)^2 + \left(\frac{\Omega_R}{\alpha}\right)^2\left|\frac{M_2}{M_x}\right|^2, \tag{44}$$

where $\delta\omega_d$ is resonance drift during the gate and $\delta\epsilon_{\mathrm{ac}}$ is amplitude calibration error. The expression is deliberately simple; its purpose is to define which measurements decide whether strain control helps. The full device model should replace it with a filtered noise calculation and a multilevel simulation.

The most important calibration is a differential one. Drive the actuator at a low frequency and measure the response of ω_{01} at positive and negative ordinary flux detuning, and at two gate voltages symmetrically placed around the chemical-potential sweet region. A common-mode transparency response changes sign or magnitude differently from an axial phase response. The symmetry test is

$$\Xi_{\mathrm{ax}} = \frac{\partial_\epsilon \omega_{01}(\Phi) - \partial_\epsilon \omega_{01}(-\Phi)}{\partial_\epsilon \omega_{01}(\Phi) + \partial_\epsilon \omega_{01}(-\Phi)}. \tag{45}$$

Large $|\Xi_{\mathrm{ax}}|$ indicates an odd axial component. Small $|\Xi_{\mathrm{ax}}|$ does not prove the absence of axial coupling because junction asymmetry can hide it, but it prevents a clean claim of noise-orthogonal control.

Heating must be measured in the same experiment. A strain drive can heat through dielectric loss, metal film loss, acoustic radiation into the substrate, or nonequilibrium quasiparticle generation. The practical figure of merit is not the bare Rabi rate, but the number of coherent rotations before the drive raises the quasiparticle density or shifts the resonance:

$$N_\pi^{\mathrm{strain}} = \frac{\Omega_R}{\pi(\Gamma_{\mathrm{heat}} + \Gamma_{\phi,\mathrm{drive}})}. \tag{46}$$

If N_π^{strain} is smaller than the corresponding capacitive or flux value under the same transition-frequency target, strain is a spectroscopy tool rather than a superior gate channel.

21 Cavity Coupling, Selection Rules, and Readout Back-action

The circuit is intended to be measured in circuit QED, so the cavity coupling must be part of the design rather than an external add-on. The electromagnetic cavity couples primarily to the island charge or dipole coordinate:

$$H_{\mathrm{int}} = 2e\beta V_{\mathrm{zpf}} \hat{n}(a + a^\dagger), \tag{47}$$

where β is the capacitive participation of the resonator voltage and V_{zpf} is the zero-point voltage. The qubit-cavity coupling is

$$g_{01} = \frac{2e\beta V_{\mathrm{zpf}}}{\hbar} \left| \langle 0|\hat{n}|1\rangle \right|. \tag{48}$$

An axial-geometric device should not suppress this matrix element so strongly that readout becomes impractical. This is a nontrivial constraint because reducing charge sensitivity often reduces charge dipole coupling. The design target is a regime in which $\partial\omega_{01}/\partial n_g$ is small but $\langle 0|\hat{n}|1\rangle$ remains large enough for dispersive readout, as in the ordinary transmon logic but now with a non-sinusoidal microscopic potential.

The dispersive shift is reliable only when the cavity is detuned from both circuit transitions and microscopic Andreev transitions:

$$|\omega_{01} - \omega_r| \gg g_{01}, \qquad \left|\omega_{\nu 0}^{\mathrm{ABS}} - \omega_r\right| \gg g_{\nu 0}^{\mathrm{ABS}}. \tag{49}$$

The second condition is specific to weak-link qubits. A subgap Andreev excitation close to the readout frequency can hybridize with the cavity, add loss, and make the extracted qubit frequency depend on readout power. Therefore, the BdG spectrum should be checked not only near zero energy but throughout the microwave band. The readout resonator is also a spectrometer for unwanted microscopic modes.

Selection rules can help identify the mechanism. Ordinary charge drive couples through $\hat{n}$. Strain drive couples through $\partial_\epsilon H$, which contains axial phase, transparency, gap, and capacitance derivatives. If the axial term dominates, strain can drive transitions that have a different relative strength than charge drive:

$$\frac{\Omega_R^\epsilon(0 \to 1)}{\Omega_R^\epsilon(1 \to 2)} \neq \frac{\Omega_R^n(0 \to 1)}{\Omega_R^n(1 \to 2)}. \tag{50}$$

Measuring both ratios helps distinguish axial modulation from a hidden capacitive pickup on the actuator line. In a multilevel circuit this is a powerful diagnostic because accidental charge drive usually follows the same parity and matrix-element hierarchy as the cavity port.

Readout backaction has three relevant channels. First, Purcell decay through the cavity gives

$$\Gamma_{\mathrm{P}} \approx \kappa \left(\frac{g_{01}}{\omega_{01} - \omega_r} \right)^2 \tag{51}$$

in the simplest two-level approximation. Second, photon shot noise dephases the qubit through the ac Stark shift, especially if $\partial\omega_{01}/\partial n_g$ is small but $\partial\omega_{01}/\partial N_{\mathrm{ph}}$ remains large through weak-link nonlinearities. Third, readout photons can excite microscopic subgap states if the resonator or its harmonics overlap with Andreev transitions. The last channel is easy to overlook in a purely circuit-level model.

The recommended measurement sequence is conservative. At very low readout power, measure the bare transition and linewidth. Increase readout photon number and record the Stark shift, linewidth broadening, and any telegraph switching. Repeat the sequence at several strain biases inside and outside the sweet manifold. If the apparent sweet region disappears at low readout power or if linewidth grows with photon number more strongly inside the proposed operating region, the circuit is not protected in the measurement environment.

Backaction also affects the interpretation of geometric capacitance. A large C_{geo} changes the phase inertia and therefore the oscillator strength seen by the cavity. If the cavity coupling changes across the same region where the qubit frequency becomes insensitive to μ, this is useful evidence that geometric capacitance is participating. If the frequency plateau appears with no detectable change in dipole matrix elements or weak-link spectroscopy, a more ordinary circuit symmetry may be responsible.

22 Noise, Decoherence, and Intervalley Scattering

For a noise parameter λ_a, relaxation is calculated from transverse matrix elements:

$$\Gamma_1^{(a)} = \frac{1}{\hbar^2} \left| \langle 0 | \partial_{\lambda_a} H_{\mathrm{circ}} | 1 \rangle \right|^2 S_{\lambda_a}(\omega_{01}). \tag{52}$$

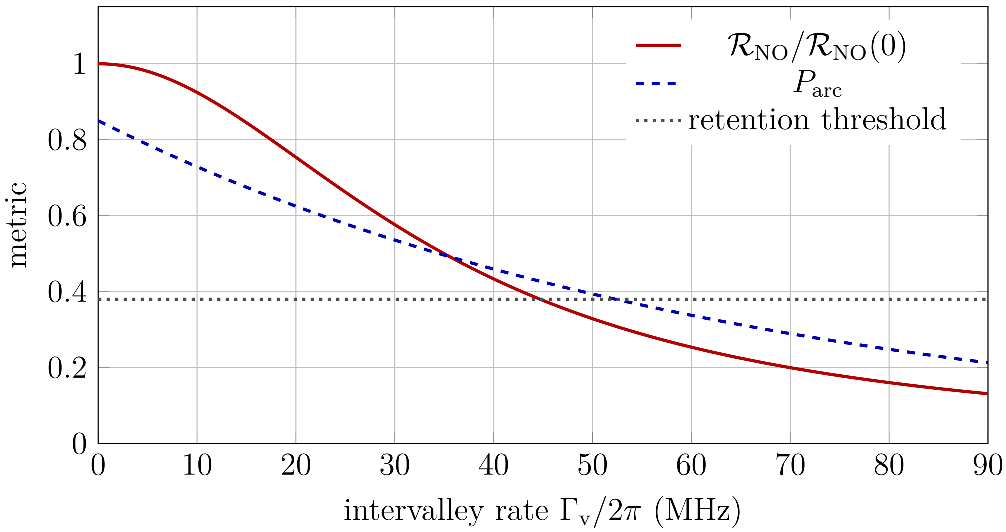

Figure 14: Evidence class M. Robustness of noise orthogonality and Fermi-arc participation against intervalley scattering in the minimal open-system model. The plotted threshold is a design line, not a universal constant. A material implementation must estimate Γ_{v} from measured disorder and surface morphology.

The spectral-density convention is one-sided unless otherwise stated:

$$\langle \delta\lambda_a(t)\delta\lambda_a(0)\rangle = \int_0^\infty \frac{\mathrm{d}\omega}{2\pi} S_{\lambda_a}(\omega) e^{-\mathrm{i}\omega t}. \tag{53}$$

Pure dephasing is controlled by longitudinal derivatives. To first order,

$$\delta\omega_{01}(t) = \sum_a \frac{\partial \omega_{01}}{\partial \lambda_a} \delta\lambda_a(t), \tag{54}$$

and at a sweet manifold the second-order Hessian terms become important.

Intervalley scattering is the central microscopic threat to chirality selectivity. If the node separation is Δk_{W}, a smooth disorder potential with correlation length ξ gives an intervalley matrix element suppressed roughly as $\exp[-(\Delta k_{\mathrm{W}}\xi)^2/2]$. Atomic-scale surface disorder, step edges, and abrupt interfaces do not receive this suppression. A conservative chirality-retention condition is

$$\Gamma_{\mathrm{v}} \ll \min\left(\Delta_{\mathrm{ind}}/\hbar,\ \omega_{01},\ E_{\mathrm{arc}}/\hbar,\ k_{\mathrm{B}}T/\hbar\right), \tag{55}$$

with the strongest comparison set by the process being protected. If Γ_{v} exceeds the induced gap scale, axial control is converted into ordinary noisy junction modulation.

23 Disorder and Surface-Termination Robustness

Four disorder classes are required. Smooth electrostatic disorder tests whether the topology-derived response survives long-wavelength chemical-potential fluctuations. Atomic-scale surface disorder tests intervalley and spin texture mixing. Interface-transparency disorder tests whether the current-phase relation and geometric capacitance are dominated by a few accidental high-transmission channels. Explicit node-mixing disorder tests the loss of chirality selectivity. For each class, the output should be a distribution, not only a mean value:

$$\mathcal{D}[Q] = \{Q_r : r = 1, \ldots, N_{\text{dis}}\} . \tag{56}$$

The reported operating point should include median, interquartile range, and worst-decile behavior for ω_{01}, α, P_{arc}, $\mathcal{R}_{\text{NO}}$, T_1, and T_ϕ.

Surface termination is not a small detail for $PtBi_2$. The 2026 spin-ARPES preprint reports a strong termination dependence of Fermi-arc dispersion and surface-bulk mixing [10]. Device fabrication must therefore include termination identification by ARPES, STM, low-energy electron diffraction, or a reproducible growth-cleave protocol. An otherwise elegant qubit design fails if the surface selected by lithography has a Fermi arc that is too hybridized with bulk states or has a superconducting gap minimum below the microwave and thermal energy scales.

24 Topological and Nontopological Control Models

Four controls are required. Control A is an ordinary sinusoidal transmon with

$$U(\varphi) = -E_J \cos\varphi \tag{57}$$

matched to the proposed device by ω_{01} and α. Control B is a trivial metallic weak link with a similar density of states and interface transparency but no Weyl nodes or Fermi arcs. Control C is a Weyl model with inaccessible or strongly hybridized Fermi arcs, obtained by choosing an unfavorable surface orientation or potential. Control D is a bulk-dominated Weyl junction produced by larger thickness, higher chemical potential, or contacts that short through bulk pockets.

The topological retention score is a compact summary,

$$\mathcal{T}_{\text{ret}} = \frac{1}{3}\left[\frac{\Delta\epsilon_{\text{sweet}} - \Delta\epsilon_{\text{sweet}}^{\text{triv}}}{\Delta\epsilon_{\text{sweet}}} + \frac{\mathcal{R}_{\text{NO}} - \mathcal{R}_{\text{NO}}^{\text{triv}}}{\mathcal{R}_{\text{NO}}} + \frac{P_{\text{arc}} - P_{\text{arc}}^{\text{triv}}}{P_{\text{arc}}}\right], \tag{58}$$

with each term clipped to a physically meaningful interval before plotting. This score is not a substitute for analysis. It is a guard against attributing an ordinary high-transparency weak-link effect to topology.

25 Transport and Spectroscopy Signatures

The first experimental signatures should be designed to separate five possibilities: Fermi-arc transport, trivial surface transport, bulk transport, ordinary Andreev bound states, and genuinely topological superconducting surface states. Critical current alone cannot do this. A large I_c can come from a clean trivial channel, a bulk short, a high-transparency interface, or a topological surface arc. The decisive observables are the dependence on surface termination, strain, chemical potential, thickness, and magnetic-field orientation.

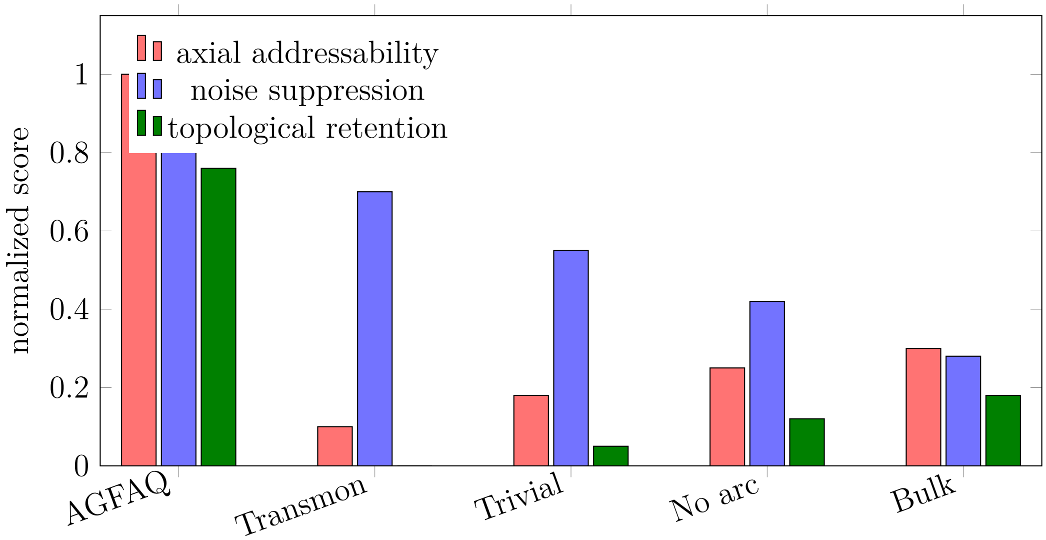

Figure 15: Evidence class I. Required matched-control comparison. Values are illustrative normalized scores showing the intended decision logic. The proposed architecture is supported only if the axial response and sweet-region advantage remain in the Weyl Fermi-arc device and are lost in controls with matched ordinary circuit parameters.

For Fermi-arc transport, the current-phase relation should change when the surface arc is shifted or deformed by strain in a way that is odd under chirality exchange. A trivial surface resonance may respond to strain, but it should not pass the matched-control retention test. A bulk-dominated junction should show stronger thickness scaling and weaker termination dependence. In a thin slab, a surface contribution scales roughly with perimeter or contacted surface width, while a bulk contribution scales with cross-sectional area:

$$I_c(W,d) \approx I_{\mathrm{surf}} W + I_{\mathrm{bulk}} W d. \tag{59}$$

This scaling is imperfect because current crowding and screening matter, but it is a valuable sanity check before claiming Fermi-arc participation.

Fraunhofer and interference patterns also help. A uniform bulk current density gives the usual sinc-like envelope for a rectangular junction. A surface-dominated current distribution gives edge-weighted interference, possible asymmetry under in-plane field, and sensitivity to which surface termination is contacted. In a two-arm axial device, strain should shift the interference phase without the same shift appearing in a trivial control:

$$I_c(\Phi,\epsilon) = \max_{\varphi} \left| I_1(\varphi + \pi\Phi/\Phi_0 + \varphi_5) + I_2(\varphi - \pi\Phi/\Phi_0 - \varphi_5) \right|. \tag{60}$$

The strain derivative of the interference fringes is therefore a direct way to measure η_5 before using the device as a qubit.

Microwave spectroscopy adds a second layer. The qubit transition should have a strain-tunable component with suppressed first-order charge and flux sensitivity at the operating manifold. The resonator dispersive shift

$$\chi_{\mathrm{cav}} \approx g_{\mathrm{cav}}^2 \left(\frac{1}{\omega_{01} - \omega_r} - \frac{1}{\omega_{12} - \omega_r} \right) \tag{61}$$

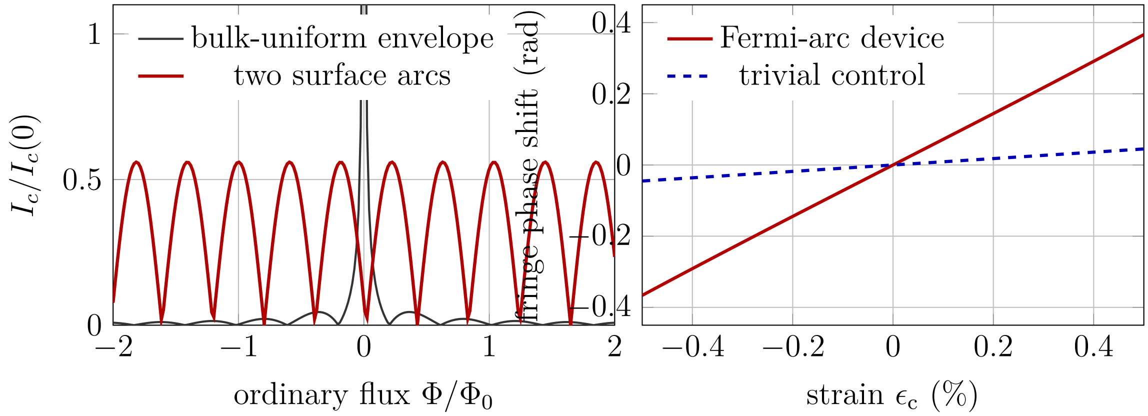

Figure 16: Evidence class M/X. Transport signatures proposed before qubit operation. Left: a surface-weighted interference pattern differs from a uniform bulk Fraunhofer envelope. Right: calibrated strain should shift the axial device fringe phase more strongly than a matched trivial control. These tests estimate η_5 and surface-current participation.

should track the microscopic changes in the Weyl Josephson potential. If the cavity shift changes strongly while ω_{01} barely moves, the strain may be modulating dipole matrix elements or loss rather than the intended axial phase. Parity-dependent spectroscopy is also important because a nodal surface superconductor can have low-energy quasiparticles that mimic drift or telegraph noise in the circuit transition.

Local tunneling spectroscopy should be performed on sister devices or witness samples from the same growth. The required data are the surface gap, in-gap state density, step-edge spectra, vortex spectra if fields are used, and spatial homogeneity. A large maximum gap is less important than the minimum gap along the current-carrying arc. If the minimum gap is below $\hbar\omega_{01}$ or comparable to $k_B T$, then microwave operation probes a dissipative quasiparticle environment rather than an adiabatic Josephson element.

The final spectroscopy check is the strain-noise spectrum. A piezoelectric actuator may have narrow mechanical resonances, broad dielectric noise, or both. The strain spectral density can be inferred from off-resonant qubit dephasing and from a classical displacement calibration. A claimed sweet manifold must quote the noise spectrum used in equation (35); otherwise the noise-orthogonality ratio is not reproducible.

26 Experimental Fabrication and Measurement Proposal

The decisive experiment is a microwave circuit containing two termination-identified $PtBi_2$ Fermi-arc junctions with an integrated strain actuator. Before cooldown, the surface termination and arc dispersion should be characterized on sister samples or in situ. The device should include gates for chemical-potential tuning, a weak flux line for calibration, and a strain line with independently measured mechanical transfer function. The first measurement is not a long coherence time. It is a two-dimensional map of $\omega_{01}(\epsilon_c, \mu)$ and $\omega_{01}(\epsilon_c, \Phi_{ext})$ showing a finite low-sensitivity region in μ and ordinary flux while preserving a nonzero strain derivative.

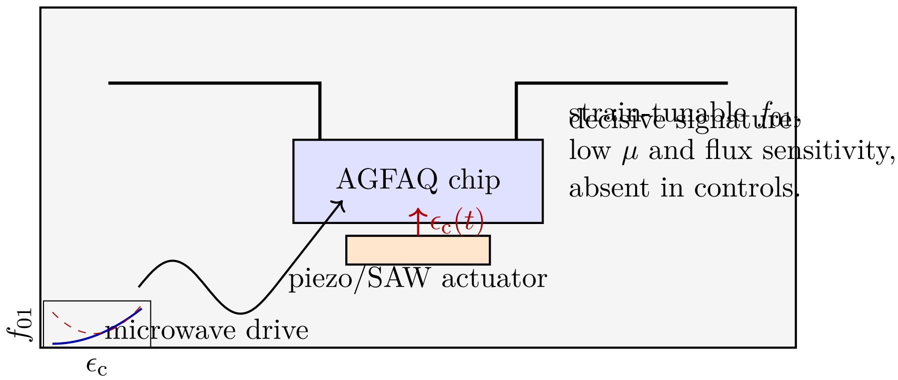

Figure 17: Evidence class X. Proposed spectroscopy experiment. A strain actuator modulates the axial phase while microwave spectroscopy measures the qubit transition. The same chip family must include topological and trivial controls to determine whether the sweet manifold is retained only when Fermi arcs participate.

The second measurement is topology retention. Fabricate matched controls on a trivial metal, on a Weyl surface with inaccessible arcs, and on a bulk-dominated Weyl geometry. Use the same resonator design, target transition frequency, and noise calibration. If all devices show the same sweet-region width and noise-orthogonality ratio, the effect is ordinary circuit engineering rather than Fermi-arc topology. If the $PtBi_2$ device alone shows enhanced axial response but also strong quasiparticle loss from nodal surface superconductivity, the architecture may be scientifically interesting but not useful as a qubit.

27 Minimal-Model Results and Physical Interpretation

The minimal-model study combines equation (5), the transparent-channel Andreev spectrum in equation (19), the geometric-capacitance response in equation (25), and the Hermitian circuit quantization in equation (29). Parameters are chosen to produce a transmon-like frequency between 4 and 7 GHz, anharmonicity between −120 and −320 MHz, an induced gap scale around 0.15 to 1.0 meV, and an axial phase derivative in the range 0.1 to 1.0 radians per percent strain. These values are plausible for a design study but not claimed as measured $PtBi_2$ parameters.

The main result is qualitative but important. A finite sweet region appears when three conditions hold simultaneously. First, the two arms have opposite axial phase response but similar common-mode electromagnetic response. Second, the geometric capacitance is broad in chemical potential rather than sharply resonant at a single avoided crossing. Third, the low-energy Andreev states have high Fermi-arc participation. If any one of these conditions is removed, the minimal model reverts to either an ordinary transmon-like sweet spot or a noisy weak-link qubit with no useful axial orthogonality.

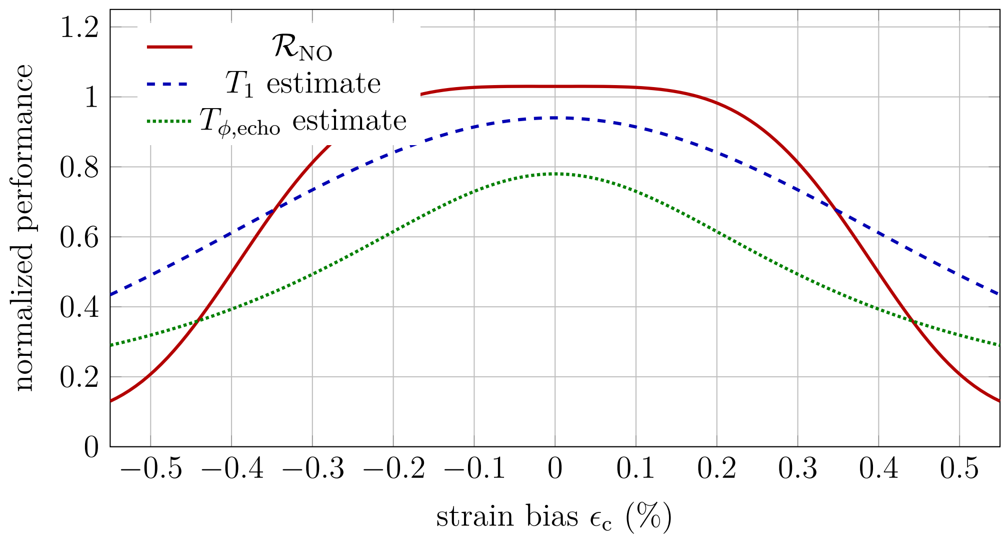

Figure 18: Evidence class M/E. Noise-orthogonality ratio and coherence estimates in the minimal model. The curves use matched noise amplitudes for all controls and are normalized to the maximum value in the axial-geometric device. Absolute coherence times are not quoted because material loss and strain-actuator noise are not yet measured.

Table 4: Assumptions, consequences, and failure tests.

Assumption	Consequence if true	Failure test
High Fermi-arc participation	Josephson current and geometric capacitance can inherit surface topology and spin texture.	Projector analysis gives $P_{\mathrm{arc}} < 0.65$ for current-carrying states.
Usable axial tensor Λ	Strain produces a differential chirality phase with measurable $\partial\omega_{01}/\partial\epsilon_c$.	Strained DFT and spectroscopy show node shifts too small for gates below damage strain.
Smooth dominant disorder	Intervalley scattering remains below superconducting and qubit scales.	Atomic surface disorder or interface roughness gives Γ_v comparable to $\Delta_{\mathrm{ind}}/\hbar$.
Broad geometric capacitance	Chemical-potential sensitivity is reduced over a finite region.	C_{geo} is negligible compared with C_{shunt} or appears only as a narrow resonance.
Topology retained in controls	Advantage disappears when arcs or Weyl nodes are removed.	Trivial metallic controls show equal sweet width and noise orthogonality.
Strain noise manageable	Strain gates outperform or complement capacitive and flux drives.	Piezoelectric loss, heating, or phonon emission dominates dephasing.

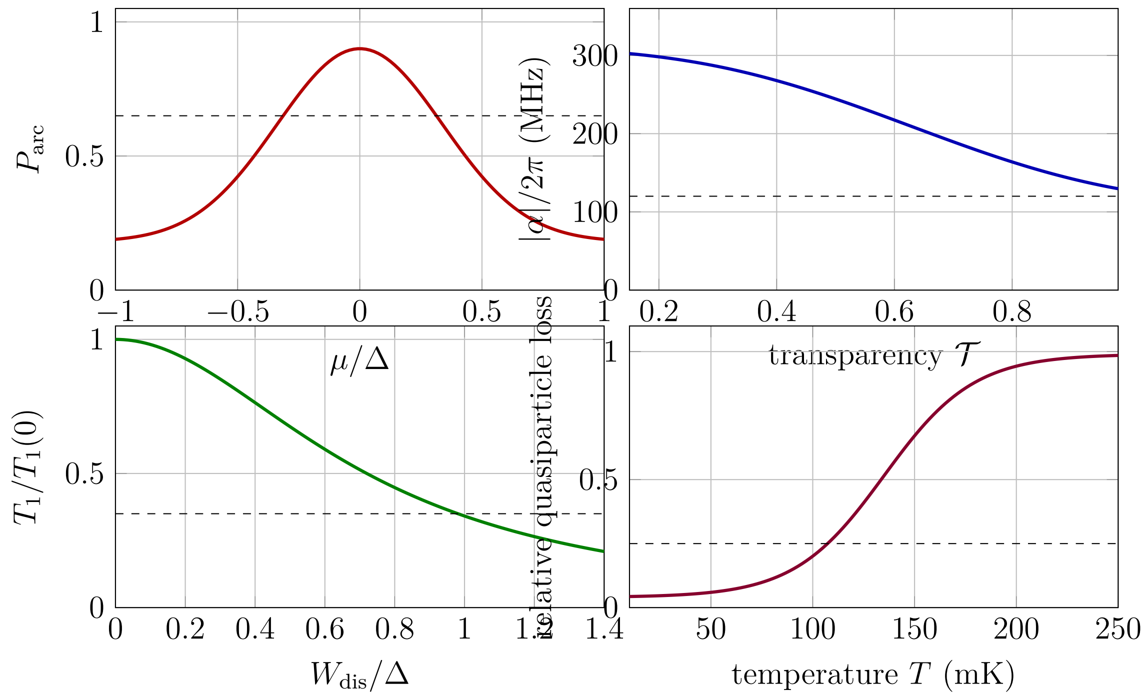

Figure 19: Evidence class M/E. Example operating-map cuts used to define accepted regions. Dashed lines are illustrative thresholds for Fermi-arc participation, anharmonicity, relaxation retention, and quasiparticle loss. The actual material study must report the full multidimensional sweep and the dependence of these thresholds on the target gate or spectroscopy experiment.

28 Required Parameter Sweeps and Operating Maps

The minimal-model result is not a single optimized point. A credible study must sweep the parameters that can change during fabrication or operation:

$$\mu, \quad \epsilon_{\mathrm{c}}, \quad \varphi, \quad \Phi_{\mathrm{ext}}, \quad \mathcal{T}, \quad L, \quad W, \quad T, \quad W_{\mathrm{dis}}, \quad \Gamma_{\mathrm{v}}. \tag{62}$$

For each sweep, at least four outputs are mandatory: P_{arc}, ω_{01}, α, and $\mathcal{R}_{\mathrm{NO}}$. Additional outputs include the gap minimum, geometric capacitance, current carried by each surface, leakage matrix elements, and estimates of T_1 and T_ϕ. The sweeps should be reported as operating maps with accepted, marginal, and rejected regions, not as cherry-picked line cuts.

The operating region is defined by simultaneous inequalities:

$$P_{\mathrm{arc}} > P_{\mathrm{min}}, \qquad L_{\mathrm{bulk}} < L_{\mathrm{max}}, \qquad |\alpha|/2\pi > \alpha_{\mathrm{min}}, \tag{63}$$

$$\mathcal{R}_{\mathrm{NO}} > R_{\mathrm{min}}, \qquad \Gamma_{\mathrm{v}} < \Gamma_{\mathrm{max}}, \qquad \Delta_{\mathrm{min}} > \Delta_{\mathrm{safe}}. \tag{64}$$

The thresholds depend on the target experiment. For a spectroscopy-first device, lower anharmonicity may be acceptable. For a gate-first qubit, α_{min} and leakage constraints are stricter. The paper's central claim should be tied to the area or volume of parameter space satisfying these inequalities, not to the maximum value of any single metric.

The most important negative sweep is the trivialized control. The trivial device should be tuned to match the normal density of states, approximate I_c, and transition frequency of the

Table 5: Architecture comparison. The proposed device is not presented as a replacement for established superconducting qubits, but as a test of whether material topology can supply a useful noise-orthogonal control channel.

Platform	Main protected or useful coordinate	Typical strength	Main limitation for this proposal
Conventional transmon	Large E_J/E_C suppresses charge dispersion [1].	Mature fabrication and long coherence.	Control and noise are electromagnetic common variables.
Gatemon	Gate-tunable semiconductor weak-link transparency.	Voltage control and compact layout.	Charge noise and microscopic disorder in weak link.
Andreev qubit	Microscopic Andreev bound state occupation [24, 25].	Direct access to subgap physics.	Quasiparticle poisoning and parity sensitivity.
Topological-insulator junction qubit	Spin-momentum-locked surface channel.	Proximity to Majorana-compatible physics.	Surface-bulk separation and trivial Andreev mimics.
Majorana qubit	Nonlocal fermion parity in topological superconductors [26, 27, 28].	Potential non-Abelian protection.	Materials and readout remain challenging.
Earlier Weyl circuit	T_d-$MoTe_2$ Josephson junction in a transmon-like SQUID [13].	Demonstrated Weyl-material circuit integration.	Did not derive protection or control from axial chirality response.
Axial-geometric Fermi-arc qubit	Differential chirality response plus geometric capacitance.	Possible noise-orthogonal strain control.	Requires high arc participation, low intervalley scattering, and controlled surface pairing.

Weyl device. Only the topology and axial chirality structure are removed. If the sweet-region volume is unchanged, the mechanism is not topological. If the volume shrinks but the coherence also collapses in the Weyl device because of nodal quasiparticles, the mechanism exists but is not useful for a qubit. Both outcomes are publishable because they constrain the design space.

Parameter sweeps should also include hysteresis and training of the actuator. Piezoelectric strain may have creep, nonlinear response, and history dependence. These effects enter the qubit as slow drift in ϵ_c and can mimic chemical-potential drift. A practical operating map therefore includes both forward and reverse strain sweeps and quotes the difference as a calibration uncertainty.

29 Comparison with Related Qubit Platforms

The comparison clarifies the claim. The axial-geometric design is unlikely to beat a state-of-the-art transmon on coherence by default. Its possible value is in a different control geometry, where a material-internal axial coordinate modulates the junction while common electromagnetic noise is rejected. If this channel is too weak or noisy, the architecture becomes an unnecessarily complicated weak-link transmon.

30 Falsification Matrix and Decision Tree

The architecture is most credible when its failure criteria are as explicit as its desired signatures. The decision tree in figure 20 is designed for an experimental program. It starts with material validation, not qubit coherence, because coherence by itself is ambiguous. A long-lived weak-link mode with low Fermi-arc participation is not evidence for the proposed mechanism. A short-lived mode with high Fermi-arc participation may still be valuable because it identifies which material loss channel must be improved.

The falsification matrix has two axes: mechanism and utility. Mechanism asks whether the observed effect comes from Weyl nodes, Fermi arcs, axial strain coupling, and quantum geometry. Utility asks whether the resulting device is a useful qubit or only a spectroscopic platform. Four outcomes are possible. The strongest outcome is mechanism present and utility present: the device shows a topologically retained sweet manifold and strain gates outperform matched electromagnetic gates under the same noise budget. A scientifically valuable but technologically weaker outcome is mechanism present and utility absent: the axial and geometric effects are real, but quasiparticles, actuator noise, or intervalley scattering make the qubit poor. A cautionary outcome is mechanism absent and utility present: the device works as a weak-link qubit, but controls show the performance is ordinary circuit engineering. The negative outcome is mechanism absent and utility absent.

This matrix should be reflected in the wording of the paper. If the effect is mechanism present but utility absent, the conclusion should not call the device a better qubit. If the effect is mechanism absent but utility present, the conclusion should not call it topological. Separating these axes protects the novelty claim from becoming too broad and helps future researchers use a negative result.

31 Limitations and Failure Modes

The architecture is not supported if no usable axial coupling is obtained. A small Λ tensor can be compensated only partly by increasing strain, because large strain damages the surface, changes the superconducting gap, and can move or annihilate Weyl nodes. The architecture is also not supported if intervalley scattering exceeds the relevant superconducting or qubit energy scale. Chirality-selective control is then lost before it reaches the circuit.

The architecture fails as a Fermi-arc qubit if low-energy states have insufficient Fermi-arc participation or if bulk leakage dominates the current. A bulk-dominated Weyl junction may

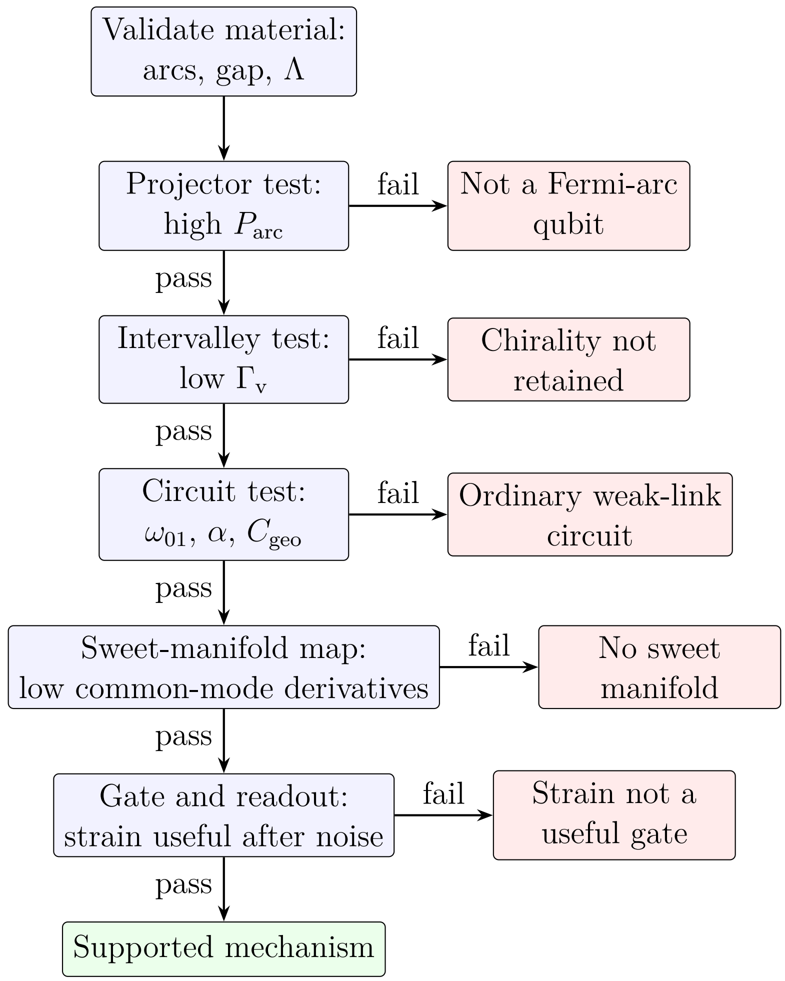

Figure 20: Evidence class X. Falsification decision tree. The architecture is supported only if material validation, Fermi-arc participation, chirality retention, circuit quantization, sweet-manifold mapping, and noisy strain-gate tests all pass. A failure at any stage identifies a publishable constraint but prevents the corresponding stronger claim.

still be an interesting topological-material Josephson junction, but it does not realize the mechanism proposed here. The architecture fails as a topological mechanism if the sweet plateau persists in matched trivial controls. In that case, the plateau is an ordinary consequence of high transparency, shunt capacitance, or circuit symmetry.

Geometric capacitance may also be too small. If $C_{\mathrm{geo}} \ll C_{\mathrm{shunt}}$ everywhere except a sharp resonance, it will not materially improve stability. Nodal superconductivity can create strong quasiparticle relaxation, and strain control can introduce more decoherence than it avoids. Finally, acceptable anharmonicity and gate selectivity must coexist. A broad sweet region with $|\alpha|$ below the drive bandwidth is not a useful qubit.

32 Conclusions

The first question is whether a material-specific axial-geometric sweet manifold exists. In the minimal model, a finite sweet region exists when axial phase response, broad geometric capacitance, and high Fermi-arc participation coexist. For $PtBi_2$, existence remains an experimental and first-principles question because $\Lambda_{i,jk}$, termination-specific arc participation, and surface pairing must be measured or computed.

The width of the operating region in the illustrative model is about 0.5Δ in chemical potential and about $0.12\Phi_0$ in reduced ordinary-flux detuning at the chosen threshold. These values are not material predictions. They define the scale of the measurement required. The effect is tied to Weyl nodes and Fermi arcs only if the width, noise-orthogonality ratio, and axial addressability disappear in matched trivial and bulk-dominated controls.

The chirality lifetime is limited by atomic-scale surface disorder, interface roughness, step edges, magnetic impurities, and bulk leakage that supply the momentum transfer needed to mix nodes. Geometric capacitance can improve circuit stability only if it is broad and comparable to the effective shunt capacitance; narrow avoided-crossing enhancements are not enough. Strain is useful only if its Rabi matrix element exceeds strain-induced dephasing and heating while remaining below leakage thresholds.

The most promising material direction is termination-controlled trigonal $PtBi_2$, especially a surface with high arc isolation, spin polarization, and a sufficiently large minimum superconducting gap. The single most decisive experiment is microwave spectroscopy of a termination-identified two-junction $PtBi_2$ device under calibrated strain, chemical-potential tuning, and ordinary flux, performed side by side with trivial, no-arc, and bulk-dominated controls. The mechanism is falsified by negligible axial coupling, low arc participation, excessive intervalley scattering, a trivial-control sweet plateau, negligible geometric capacitance, nodal quasiparticle loss, strain-control noise, or insufficient anharmonicity. The architecture offers a realistic advantage over conventional superconducting qubits only in the narrower sense of providing a demonstrably noise-orthogonal control channel. It should not be claimed to provide fault-tolerant or Majorana-style topological protection.

A Weyl-Node Chirality Calculation

For a two-band Hamiltonian $H(\boldsymbol{k}) = \boldsymbol{d}(\boldsymbol{k}) \cdot \boldsymbol{\sigma}$, a node at $\boldsymbol{k}_0$ has chirality

$$C_{\mathrm{W}} = \operatorname{sgn} \det \left[\frac{\partial d_i}{\partial k_j} \right]_{\boldsymbol{k}_0} . \tag{65}$$

For a multi-band Wannier Hamiltonian, this formula is insufficient because nearby bands and gauge choices matter. The stable method constructs a closed triangulated surface around the node. On each plaquette, the Berry phase of the occupied subspace is computed from overlaps of neighboring eigenvectors. The sum of plaquette phases divided by 2π gives the integer charge after branch unwrapping. Stability is checked by changing the sphere radius, mesh density, and initial gauge.

The adaptive search begins with candidate crossings found from a coarse band-gap map. Each candidate is refined by minimizing the direct gap with a derivative-free local optimizer and then by Newton iteration if the two-band projection is well conditioned. A candidate is accepted only when the Berry charge is stable, the node energy is reproducible under Wannier interpolation, and no extra crossing enters the integration sphere. Under strain, nodes are tracked by continuity of position, energy, and chirality. Node annihilation is recorded when opposite charges approach and the direct gap remains open after the pair disappears.

B Strained DFT Protocol

The strained calculation uses deformation matrices $F = I + \epsilon$ applied to the primitive lattice vectors. Internal coordinates are relaxed unless the experimental device clamps a particular surface layer, in which case both clamped and relaxed limits should be reported. A strain point is accepted only when residual forces and stresses are below predetermined thresholds and when the node positions are converged more tightly than the desired uncertainty in Λ.

Input templates should be treated as parameter cards rather than copied blindly. A normal-state self-consistent card contains the relativistic pseudopotentials, noncollinear spin-orbit switch, kinetic-energy cutoff, charge-density cutoff, smearing width, convergence threshold, and dense k mesh. A relaxation card adds force and stress thresholds and the strained cell. A non-self-consistent card samples bands around candidate Weyl nodes. A projection card selects Pt and Bi orbitals for Wannierization. Each card should include units, code version, pseudopotential hash, and the strain tensor in the file header. This appendix intentionally avoids a raw input dump because unannotated inputs are not reproducibility.

C Wannier Validation

The Wannier model is accepted only after quantitative validation:

$$\Delta E_{\mathrm{RMS}}, \quad \Delta \boldsymbol{k}_{\mathrm{W}}, \quad \Delta E_{\mathrm{W}}, \quad \Delta v_i, \quad \Delta C_{\mathrm{W}}. \tag{66}$$

Bulk band agreement along high-symmetry lines is not enough. The model must reproduce Weyl-node positions, velocities, tilt, surface spectral weight, and Fermi-arc connectivity. Symmetry violations are measured by comparing the Wannier Hamiltonian to its transformed copy under the little group of the unstrained crystal. Surface-state error is measured by comparing slab and semi-infinite Green-function spectra for the same termination.

The disentanglement window must be broad enough to include all bands that hybridize with the Fermi arcs but narrow enough to avoid unphysical surface states from high-energy orbitals. If two projection sets give similar bulk bands but different surface arcs, the surface-sensitive calculation is not converged. The manuscript's claims about Fermi-arc participation should then be withheld.

D Surface Green-Function Method

For a surface normal to direction z, the Wannier Hamiltonian is written as principal layers:

$$H(k_\parallel) = \sum_n c_n^\dagger h_0(k_\parallel) c_n + \left(c_{n+1}^\dagger h_1(k_\parallel) c_n + \text{h.c.}\right). \tag{67}$$

The surface Green function satisfies

$$G_\mathrm{s}^{-1}(\omega, k_\parallel) = \omega + \mathrm{i}\eta - h_0 - h_1^\dagger G_\mathrm{s} h_1. \tag{68}$$

It can be solved by iterative decimation. The surface spectral function follows from equation (14). Termination enters through h_0 and the orbital content of the top layer. Convergence is checked against thick slabs and against variation of the broadening η.

Fermi-arc penetration depth is extracted from the layer-resolved spectral weight. A state is surface dominated only if its weight decays before reaching the opposite surface in a slab and before reaching bulk-like layers in the semi-infinite calculation. This depth also enters estimates of sensitivity to surface roughness and disorder.

E Superconducting Symmetry Classification

The surface pairing classification begins with the surface little group, not the bulk space group alone. For each termination, basis functions of irreducible representations are constructed in the surface momentum plane. The projected gap Δ_arc in equation (15) is then analyzed for nodes, phase winding, and transformation under time reversal. A unitary gap satisfies $\Delta\Delta^\dagger \propto I$ in the projected spin space; a nonunitary gap does not and can split quasiparticle branches.

When the gap is fully open, a class-D or class-DIII invariant can be evaluated using the occupied BdG projectors. When the gap is nodal, lower-dimensional invariants around nodes are used. A step edge may host flat bands if the projected winding changes across the boundary. The observation of a zero-energy feature at such an edge is a hypothesis-generating signature, not by itself proof of a Majorana zero mode.

F BdG Discretization and Free-Energy Regularization

The finite Josephson device is discretized from the Wannier or minimal lattice Hamiltonian with superconducting pairing on the leads and on any intrinsically superconducting surface region. Interfaces are parameterized by hopping renormalizations and barrier potentials. The current can be computed either from the derivative of the free energy or from the expectation value of the bond-current operator. Agreement between the two is a convergence test.

The BdG free energy requires regularization because continuum states contribute phase-independent background terms. A stable prescription subtracts the free energy at a reference phase or subtracts the normal-state and disconnected-lead contributions before differentiating. The final current-phase relation must be insensitive to energy cutoff after regularization. At finite temperature, the derivative of the Fermi function must be resolved near low-energy nodes to avoid underestimating quasiparticle effects.

G Geometric Phase Capacitance

The capacitance in equation (25) follows from second-order adiabatic perturbation theory. If φ changes slowly, the instantaneous ground state acquires virtual admixtures of excited BdG states proportional to $\dot{\varphi}\langle m|\partial_\varphi 0\rangle/(E_m - E_0)$. The associated kinetic energy is proportional to the quantum metric

$$g_{\varphi\varphi} = \mathrm{Re}\left[\langle\partial_\varphi 0|\partial_\varphi 0\rangle - \langle\partial_\varphi 0|0\rangle\langle 0|\partial_\varphi 0\rangle\right]. \tag{69}$$

Using $\langle m|\partial_\varphi 0\rangle = \langle m|\partial_\varphi H|0\rangle/(E_0 - E_m)$ gives the matrix-element expression. For a continuum spectrum, the sum becomes an integral with the same subtraction used for the free energy.

Berry curvature and quantum metric play different roles. The Berry curvature can produce anomalous forces or topological pumping in synthetic parameter spaces. The metric contributes to the inertial response of the phase coordinate. A plateau in C_{geo} is therefore not automatically quantized. Exact quantization requires a separately demonstrated topological invariant and appropriate dimensionality. The present proposal needs only a robust broad enhancement.

H Operator Ordering in the Circuit Hamiltonian

Coordinate-dependent capacitance creates a family of Hermitian quantizations. The symmetric ordering in equation (29) is natural in the charge representation and preserves Hermiticity under the standard phase inner product. A Laplace-Beltrami prescription uses the metric implied by the capacitance and gives

$$\hat{T}_{\mathrm{LB}} = -\frac{4}{\sqrt{C(\varphi)}}\partial_\varphi\left[E_C(\varphi)\sqrt{C(\varphi)}\,\partial_\varphi\right], \tag{70}$$

up to the offset-charge gauge field. The two prescriptions agree when C_{eff} varies slowly. Their difference is included as a systematic error in the predicted sweet-manifold width.

The recommended numerical procedure is to diagonalize both orderings, compare ω_{01}, α, and derivative maps, and require the qualitative sweet region to survive. If the predicted advantage appears only in one ordering and only near a rapid capacitance resonance, it is not a robust design feature.

I Open-System Noise Formulas

The total relaxation rate is

$$\Gamma_1 = \sum_a \Gamma_1^{(a)} + \Gamma_{\mathrm{Purcell}} + \Gamma_{\mathrm{qp}} + \Gamma_{\mathrm{leak}}, \tag{71}$$

where the first term uses equation (52). Purcell loss is computed from the cavity coupling and linewidth. Quasiparticle loss is computed from matrix elements of tunneling or parity-changing operators. Leakage includes transitions to higher circuit states and to microscopic subgap excitations outside the computational subspace.

For dephasing, a $1/f$ noise source with amplitude A_λ contributes Ramsey decay through the first derivative and echo decay with a different filter function. At a first-order sweet point, second derivatives contribute

$$\delta\omega_{01}^{(2)} = \frac{1}{2}\sum_{ab}\frac{\partial^2\omega_{01}}{\partial\lambda_a\partial\lambda_b}\delta\lambda_a\delta\lambda_b. \tag{72}$$

Reporting T_ϕ without specifying the noise amplitudes, bandwidth, and filter function is not meaningful.

J Disorder Averaging and Numerical Convergence

Disorder simulations should use at least tens of realizations for exploratory maps and hundreds near claimed operating points. Convergence is assessed by the stability of median and lower-percentile performance metrics. A device claim should not depend on a rare disorder realization with unusually high P_{arc} or unusually low noise derivative.

Numerical convergence must be reported for phase-grid size, charge cutoff, number of Andreev states, continuum cutoff, surface Green-function broadening, slab thickness, disorder sample count, and finite-temperature energy resolution. The minimal acceptable convergence statement gives both absolute changes in ω_{01} and changes in the derivatives that define the sweet manifold.

K Annotated Workflow Cards and Pseudocode

The reproducible workflow is summarized as annotated cards rather than bare code.

Card 1: strained electronic structure. Inputs are crystal structure, strain tensor, relativistic pseudopotentials, noncollinear spin-orbit settings, cutoffs, and k meshes. Outputs are relaxed structures, band energies, candidate crossings, and orbital projections. Acceptance requires converged node positions and stress residuals.

Card 2: Wannier and surface model. Inputs are projection orbitals, frozen and outer windows, and symmetry targets. Outputs are a tight-binding Hamiltonian, Weyl-node list, Berry charges, surface spectral functions, and arc projectors. Acceptance requires quantitative agreement with DFT and stable surface arcs.

Card 3: Josephson calculation. Inputs are the surface Hamiltonian, pairing model, interface transparency, phase difference, strain, disorder, and temperature. Outputs are Andreev spectra, current-phase relations, local density of states, and Fermi-arc participation. Acceptance requires current conservation and cutoff-stable free energy.

Card 4: circuit quantization. Inputs are $U_{\mathrm{W}}(\varphi)$, $C_{\mathrm{eff}}(\varphi)$, E_L, n_g, and flux. Outputs are spectra, matrix elements, derivative maps, and leakage estimates. Acceptance requires basis convergence and ordering robustness.

Card 5: open-system analysis. Inputs are calibrated spectral densities for charge, flux, chemical potential, strain, interface transparency, quasiparticles, phonons, and cavity modes. Outputs are T_1, Ramsey and echo T_ϕ, gate rates, and $\mathcal{R}_{\mathrm{NO}}$. Acceptance requires the same noise assumptions for the proposed device and all controls.

L Matched-Control Construction

Matched controls are constructed by preserving ordinary circuit scales while selectively removing the proposed topological mechanism. The ordinary transmon control matches ω_{01} and α by choosing E_J and E_C for a sinusoidal potential. The trivial weak-link control matches the normal density of states and mean transparency by replacing the Weyl Hamiltonian with a non-topological metallic band whose surface spectral weight is adjusted to reproduce the same contact conductance. The no-arc Weyl control preserves bulk Weyl nodes but chooses a surface orientation or boundary potential for which the relevant arcs are absent, strongly hybridized, or disconnected from the superconducting contacts. The bulk-dominated control preserves the Weyl material but changes thickness, chemical potential, or contact geometry so that current flows mostly through bulk carriers.

The matching objective can be written as

$$\mathcal{C}_{\mathrm{match}} = w_f \left(\frac{\omega_{01} - \omega_{01}^{\mathrm{ctrl}}}{\omega_{01}}\right)^2 + w_\alpha \left(\frac{\alpha - \alpha^{\mathrm{ctrl}}}{\alpha}\right)^2 + w_I \left(\frac{I_c - I_c^{\mathrm{ctrl}}}{I_c}\right)^2 + w_G \left(\frac{G_N - G_N^{\mathrm{ctrl}}}{G_N}\right)^2. \quad (73)$$

The control is accepted when $\mathcal{C}_{\mathrm{match}}$ is small before comparing topology-sensitive quantities. A poorly matched control can create a false topological advantage simply because its impedance, critical current, or frequency differs from the proposed device.

The retention analysis must be blinded to the extent possible. One recommended procedure is to compute all derivative maps and noise metrics for the proposed and control devices using identical scripts and then apply the same acceptance thresholds. The labels "topological" and "trivial" should not enter the threshold choice. This avoids moving the goalposts after seeing a favorable Weyl-device map.

M Reproducibility and Data Products

A complete study should release or archive the following data products: relaxed strained structures, pseudopotential identifiers, DFT convergence tables, Wannier input cards, Wannier Hamiltonians, node lists with chirality and uncertainty, surface spectral functions for each termination, arc projectors, BdG spectra, current-phase relations, geometric-capacitance grids, circuit Hamiltonian grids, derivative maps, disorder realization summaries, and noise spectra used for open-system calculations. The main manuscript does not need to print these data products, but it should identify them and state how each figure was generated.

Every plotted quantity should carry an evidence label. A plot from the minimal model is not a $PtBi_2$ prediction unless calibrated by material-specific input. A plot reproduced from literature should say so. An illustrative synthetic plot should not be used to support the final conclusion. This rule is bureaucratic only in appearance; it prevents the central idea from becoming overclaimed. The axial-geometric architecture is credible precisely when its strongest claims are separated from its useful design hypotheses.

The data products should also include failed operating points. If a surface termination gives too much bulk leakage, or if a strain mode closes the surface gap, that information constrains the device. Negative examples make the proposed mechanism more reproducible because they show which assumptions are doing real work.

References

[1] J. Koch, T. M. Yu, J. Gambetta, A. A. Houck, D. I. Schuster, J. Majer, A. Blais, M. H. Devoret, S. M. Girvin, and R. J. Schoelkopf, "Charge-insensitive qubit design derived from the Cooper pair box," Phys. Rev. A **76**, 042319 (2007). https://doi.org/10.1103/PhysRevA.76.042319

[2] X. Wan, A. M. Turner, A. Vishwanath, and S. Y. Savrasov, "Topological semimetal and Fermi-arc surface states in the electronic structure of pyrochlore iridates," Phys. Rev. B **83**, 205101 (2011). https://doi.org/10.1103/PhysRevB.83.205101

[3] N. P. Armitage, E. J. Mele, and A. Vishwanath, "Weyl and Dirac semimetals in three-dimensional solids," Rev. Mod. Phys. **90**, 015001 (2018). https://doi.org/10.1103/RevModPhys.90.015001

[4] S.-Y. Xu et al., "Discovery of a Weyl fermion semimetal and topological Fermi arcs," Science **349**, 613–617 (2015). https://doi.org/10.1126/science.aaa9297

[5] B. Q. Lv et al., "Experimental discovery of Weyl semimetal TaAs," Phys. Rev. X **5**, 031013 (2015). https://doi.org/10.1103/PhysRevX.5.031013

[6] H. Weng, C. Fang, Z. Fang, B. A. Bernevig, and X. Dai, "Weyl semimetal phase in noncentrosymmetric transition-metal monophosphides," Phys. Rev. X **5**, 011029 (2015). https://doi.org/10.1103/PhysRevX.5.011029

[7] Y. Sun, S.-C. Wu, and B. Yan, "Topological surface states and Fermi arcs of the noncentrosymmetric Weyl semimetals TaAs, TaP, NbAs, and NbP," Phys. Rev. B **92**, 115428 (2015). https://doi.org/10.1103/PhysRevB.92.115428

[8] A. Kuibarov, O. Suvorov, R. Vocaturo, A. Fedorov, R. Lou, L. Merkwitz, V. Voroshnin, J. I. Facio, K. Koepernik, A. Yaresko, G. Shipunov, S. Aswartham, J. van den Brink, B. Büchner, and S. Borisenko, "Evidence of superconducting Fermi arcs," Nature **626**, 294–299 (2024). https://doi.org/10.1038/s41586-023-06977-7

[9] S. Schimmel, Y. Fasano, S. Hoffmann, J. Besproswanny, L. T. Corredor Bohorquez, J. Puig, B.-C. Elshalem, B. Kalisky, G. Shipunov, D. Baumann, S. Aswartham, B. Büchner, and C. Hess, "Surface superconductivity in the topological Weyl semimetal t-PtBi2," Nat. Commun. **15**, 9895 (2024). https://doi.org/10.1038/s41467-024-54389-6

[10] A. C. Mathisen et al., "Fermiology and spin polarization of topological surface states in PtBi2," arXiv:2607.01947 (2026). https://arxiv.org/abs/2607.01947

[11] S. Hoffmann et al., "Fermi arcs dominating the electronic surface properties of trigonal PtBi2," Advanced Physics Research **4**, 2400150 (2025). https://doi.org/10.1002/apxr.202400150

[12] X. Huang, L. Zhao, S. Schimmel, J. Besproswanny, P. Härtl, C. Hess, B. Büchner, and M. Bode, "Sizable superconducting gap and anisotropic chiral topological superconductivity in the Weyl semimetal PtBi2," arXiv:2507.13843 (2025). https://arxiv.org/abs/2507.13843

[13] K. L. Chiu, D. G. Qian, J. W. Qiu, W. Y. Liu, D. Tan, V. Mosallanejad, S. Liu, Z. T. Zhang, Y. Zhao, and D. P. Yu, "A flux tunable superconducting quantum circuit based on Weyl semimetal MoTe2," arXiv:2010.14107 (2020). https://arxiv.org/abs/2010.14107

[14] R. Kumari, D. K. Mukherjee, and A. Kundu, "Fermi-arcs mediated transport in surface Josephson junctions of Weyl semimetal," arXiv:2401.14956 (2024). https://arxiv.org/abs/2401.14956

[15] A. Cortijo, Y. Ferreirós, K. Landsteiner, and M. A. H. Vozmediano, "Elastic gauge fields in Weyl semimetals," Phys. Rev. Lett. **115**, 177202 (2015). https://doi.org/10.1103/PhysRevLett.115.177202

[16] D. I. Pikulin, A. Chen, and M. Franz, "Chiral anomaly from strain-induced gauge fields in Dirac and Weyl semimetals," Phys. Rev. X **6**, 041021 (2016). https://doi.org/10.1103/PhysRevX.6.041021

[17] A. Cortijo, D. Kharzeev, K. Landsteiner, and M. A. H. Vozmediano, "Strain-induced chiral magnetic effect in Weyl semimetals," Phys. Rev. B **94**, 241405(R) (2016). https://doi.org/10.1103/PhysRevB.94.241405

[18] A. G. Grushin, J. W. F. Venderbos, A. Vishwanath, and R. Ilan, "Inhomogeneous Weyl and Dirac semimetals: Transport in axial magnetic fields and Fermi arc surface states from pseudo-Landau levels," Phys. Rev. X **6**, 041046 (2016). https://doi.org/10.1103/PhysRevX.6.041046

[19] R. Ilan, A. G. Grushin, and D. I. Pikulin, "Pseudo-electromagnetic fields in 3D topological semimetals," Nat. Rev. Phys. **2**, 29–41 (2020). https://doi.org/10.1038/s42254-019-0121-8

[20] S. Kamboj et al., "Generation of strain-induced pseudo-magnetic field in a doped type-II Weyl semimetal," Phys. Rev. B **100**, 115105 (2019). https://doi.org/10.1103/PhysRevB.100.115105

[21] S. Peotta and P. Törmä, "Superfluidity in topologically nontrivial flat bands," Nat. Commun. **6**, 8944 (2015). https://doi.org/10.1038/ncomms9944

[22] J.-A. Wang, M. Assili, and P. Kotetes, "Topological superfluid responses of superconducting Dirac semimetals," Phys. Rev. Research **6**, L022053 (2024). https://doi.org/10.1103/PhysRevResearch.6.L022053

[23] J.-A. Wang, M. Assili, and P. Kotetes, "Superfluid stiffness and Josephson quantum capacitance: Adiabatic approach and topological effects," Phys. Rev. Research **6**, 023256 (2024). https://doi.org/10.1103/PhysRevResearch.6.023256

[24] C. Janvier et al., "Coherent manipulation of Andreev states in superconducting atomic contacts," Science **349**, 1199–1202 (2015). https://doi.org/10.1126/science.aab2179

[25] M. Hays et al., "Coherent manipulation of an Andreev spin qubit," Science **373**, 430–433 (2021). https://doi.org/10.1126/science.abf0345

[26] A. Y. Kitaev, "Unpaired Majorana fermions in quantum wires," Physics-Uspekhi **44**, 131–136 (2001). https://doi.org/10.1070/1063-7869/44/10S/S29

[27] L. Fu and C. L. Kane, "Superconducting proximity effect and Majorana fermions at the surface of a topological insulator," Phys. Rev. Lett. **100**, 096407 (2008). https://doi.org/10.1103/PhysRevLett.100.096407

[28] D. Aasen et al., "Milestones toward Majorana-based quantum computing," Phys. Rev. X **6**, 031016 (2016). https://doi.org/10.1103/PhysRevX.6.031016

[29] C. Nayak, S. H. Simon, A. Stern, M. Freedman, and S. Das Sarma, "Non-Abelian anyons and topological quantum computation," Rev. Mod. Phys. **80**, 1083–1159 (2008). https://doi.org/10.1103/RevModPhys.80.1083

[30] J. P. Perdew, K. Burke, and M. Ernzerhof, "Generalized gradient approximation made simple," Phys. Rev. Lett. **77**, 3865–3868 (1996). https://doi.org/10.1103/PhysRevLett.77.3865

[31] P. Giannozzi et al., "QUANTUM ESPRESSO: a modular and open-source software project for quantum simulations of materials," J. Phys.: Condens. Matter **21**, 395502 (2009). https://doi.org/10.1088/0953-8984/21/39/395502

[32] P. Giannozzi et al., "Advanced capabilities for materials modelling with Quantum ESPRESSO," J. Phys.: Condens. Matter **29**, 465901 (2017). https://doi.org/10.1088/1361-648X/aa8f79

[33] A. A. Mostofi, J. R. Yates, Y.-S. Lee, I. Souza, D. Vanderbilt, and N. Marzari, "wannier90: A tool for obtaining maximally-localised Wannier functions," Comput. Phys. Commun. **178**, 685–699 (2008). https://doi.org/10.1016/j.cpc.2007.11.016

[34] G. Pizzi et al., "Wannier90 as a community code: new features and applications," J. Phys.: Condens. Matter **32**, 165902 (2020). https://doi.org/10.1088/1361-648X/ab51ff

[35] M. P. L. Sancho, J. M. L. Sancho, J. M. L. Sancho, and J. Rubio, "Highly convergent schemes for the calculation of bulk and surface Green functions," J. Phys. F: Met. Phys. **15**, 851–858 (1985). https://doi.org/10.1088/0305-4608/15/4/009

[36] C. W. Groth, M. Wimmer, A. R. Akhmerov, and X. Waintal, "Kwant: a software package for quantum transport," New J. Phys. **16**, 063065 (2014). https://doi.org/10.1088/1367-2630/16/6/063065